Quaternary Science Reviews 113 (2015) 171–192

Contents lists available at ScienceDirect

Quaternary Science Reviews

journal homepage: www.elsevier.com/locate/quascirev

Segmentation of the 2010 Maule Chile earthquake rupture from a joint analysis of uplifted marine terraces and seismic-cycle deformation patterns

Julius Jara-Muñoz [a, *], Daniel Melnick [a], Dominik Brill [b], Manfred R. Strecker [a]

[a] Institut für Erd- und Umweltwissenschaften, Universität Potsdam, 14476 Potsdam, Germany
[b] Geographisches Institut, Universität Köln, 50923 Köln, Germany

ARTICLE INFO

Article history:
Received 31 May 2014
Received in revised form
4 November 2014
Accepted 8 January 2015
Available online 7 February 2015

Keywords:
LiDAR
Subduction earthquakes
Marine terraces
Seismotectonic segmentation
Permanent uplift
Maule earthquake
Coastal uplift
TerraceM

ABSTRACT

The segmentation of major fault systems in subduction zones controls earthquake magnitude and location, but the causes for the existence of segment boundaries and the relationships between long-term deformation and the extent of earthquake rupture, are poorly understood. We compare permanent and seismic-cycle deformation patterns along the rupture zone of the 2010 Maule earthquake (M8.8), which ruptured 500 km of the Chile subduction margin. We analyzed the morphology of MIS-5 marine terraces using LiDAR topography and established their chronology and coeval origin with twelve luminescence ages, stratigraphy and geomorphic correlation, obtaining a virtually continuous distribution of uplift rates along the entire rupture zone. The mean uplift rate for these terraces is 0.5 m/ka. This value is exceeded in three areas, which have experienced rapid emergence of up to 1.6 m/ka; they are located at the northern, central, and southern sectors of the rupture zone, referred to as Topocalma, Carranza and Arauco, respectively. The three sectors correlate with boundaries of eight great earthquakes dating back to 1730. The Topocalma and Arauco sectors, located at the boundaries of the 2010 rupture, consist of broad zones of crustal warping with wavelengths of 60 and 90 km, respectively. These two regions coincide with the axes of oroclinal bending of the entire Andean margin and correlate with changes in curvature of the plate interface. Rapid uplift at Carranza, in turn, is of shorter wavelength and associated with footwall flexure of three crustal-scale normal faults. The uplift rate at Carranza is inversely correlated with plate coupling as well as with coseismic slip, suggesting permanent deformation may accumulate interseismically. We propose that the zones of upwarping at Arauco and Topocalma reflect changes in frictional properties of the megathrust resulting in barriers to the propagation of great earthquakes. Slip during the 1960 (M9.5) and 2010 events overlapped with the ~90-km-long zone of rapid uplift at Arauco; similarly, slip in 2010 and 1906 extended across the ~60-km-long section of the megathrust at Topocalma, but this area was completely breached by the 1730 (M~9) event, which propagated southward until Carranza. Both Arauco and Topocalma show evidence of sustained rapid uplift since at least the middle Pleistocene. These two sectors might thus constitute discrete seismotectonic boundaries restraining most, but not all great earthquake ruptures. Based on our observations, such barriers might be breached during multi-segment super-cycle events.

1. Introduction

The seismic cycle of great subduction earthquakes has been described as a repetitive sequence of crustal deformation phenomena constituting three main steps: strain accumulation during the inter-seismic period, release of strain by an earthquake during the co-seismic stage, and the post-seismic period, characterized by complex transient processes in the years to decades following the earthquake (e.g. Wang, 2007). The cumulative, permanent deformation, which is expressed in mountain building and the formation of sedimentary basins, integrates this cycle over long timescales. The pioneering observations of co-seismic uplift during the 1835 Chile earthquake by Darwin and FitzRoy are considered to be the first empirical confirmation of the relationship between

* Corresponding author.
E-mail address: jara@geo.uni-potsdam.de (J. Jara-Muñoz).

http://dx.doi.org/10.1016/j.quascirev.2015.01.005
0277-3791/

earthquakes and mountain building (Darwin, 1851; Kölbl-Ebert, 1999). However, neither the spatial nor the temporal relationships between both processes – the different steps of the seismic cycle and mountain building – are fully understood.

It has been proposed that forearc regions are divided into semi-independent seismotectonic segments. Such segments may reflect the long-term structural and topographic expression of numerous earthquake cycles, thus forming geomorphic entities that sustain their style and rate of deformation over long timescales (e.g. Ando, 1975; Taylor et al., 1987; Chen et al., 2011; Victor et al., 2011). This notion is partly based on the observation that the slip distribution of some great to giant (M 8–9) megathrust earthquakes exhibits a clear segmentation into distinct sectors. Examples include the 1964 Alaska (Suito and Freymueller, 2009), 2004 Sumatra (Chlieh et al., 2007), and the 1960 and 2010 Chile (Moreno et al., 2009, 2012) earthquakes. In contrast to these observations, slip during the 2011 Tohoku (M9.1) event in Japan was rather localized in a single region (Ozawa et al., 2011).

Slip distributions of the 1960 Chile (M9.5) and the 2011 Tohoku (M9.1) earthquakes exhibit a certain degree of coherence with the pattern of pre-seismic locking determined from modeling of geodetic data (Moreno et al., 2010; Loveless and Meade, 2011; Moreno et al., 2012). Despite these recent advances in assessing the mechanics of slip distribution and how deformation is accrued in repeated large earthquakes, the correlations between co-seismic slip and the sustained long-term segmentation of forearcs, particularly in Chile, remain poorly understood. In addition, it is not known why forearcs may rupture repeatedly along the full length of segments (e.g. Shennan et al., 2009) or why ruptures propagate across segment boundaries under certain circumstances (e.g. Nanayama et al., 2003; Taylor et al., 2008). Gaining insight into the mechanical causes for segmentation, rupture propagation, and the characteristics of seismic-cycle vs. permanent deformation patterns of forearcs may help define the stable or transient nature of forearc-segment boundaries and furnish information vital to seismic hazard assessments.

In an attempt to contribute to this important topic we studied marine terrace systems, which occur at different elevations along the Chile margin. Multiple flights of marine terrace systems are ideal geomorphic strain markers that allow for an analysis of surface-uplift rates, spatiotemporal variation in deformation and uplift patterns, and the characteristics of potential forearc segmentation (e.g. Lajoie, 1986; Pedoja et al., 2011). In this study we use detailed geologic mapping, morphometric analysis, and age determinations of interglacial marine terraces to assess long-term seismotectonic segmentation in light of the ~500-km-long rupture zone of the 2010 Maule (M8.8) earthquake along the south-central part of the Chile convergent margin.

Over the last decade earthquake research has benefited from the availability of LiDAR (light detection and ranging) topographic data, which allows producing a vegetation-free surface digital terrain models. Here we use such bare-earth models to analyze terrace sequences along the entire Maule rupture. Based on age determinations as well as stratigraphic and morphologic criteria, we correlate marine terraces along the rupture zone to obtain virtually continuous uplift rate estimates spanning the past ~10^5 years. Furthermore, we compare the pattern of uplift rates and their gradients with the extent of historical megathrust earthquakes and co-seismic slip distribution during the Maule earthquake and interseismic coupling in the decade before the event. Based on these correlations, we infer the relation between the position and nature of earthquake barriers, proposing a seismotectonic segmentation comprising persistent and transient boundaries in the realm of the Maule earthquake in south-central Chile.

2. Tectonic and geomorphic framework

2.1. Regional tectonic and geologic setting

Coastal south-central Chile is an integral part of the tectonically active forearc, where the oceanic Nazca plate is subducted beneath the South American continent at a convergence rate of 66 mm/yr (Angermann et al., 1999). The age of the Nazca plate along the Maule rupture increases continuously northward, from ~25 to 32 My (Tebbens and Cande, 1997). This segment of the margin has been in an accretionary tectonic mode since the Pliocene (Bangs and Cande, 1997), with a frontal accretionary wedge extending ~60 km inland from the trench along the continental slope and limited by a system of landward-dipping splay faults (Geersen et al., 2011) (Fig. 1B). The continental platform includes several up to ~3-km-deep Cenozoic forearc basins, which taper toward the slope and coast (e.g. Mordojovich, 1981).

Onshore, the main morphotectonic province is the Coastal Range. Its core includes a high-pressure Paleozoic accretionary complex intruded by a granitic batholith (Fig. 1B) (Kato, 1985). Limited exposures of forearc basins at the western flank of the Coastal Range consist of Cretaceous to Quaternary marine and continental sedimentary sequences in three main depocenters bounded by basement highs: the Arauco, Carranza, and Topocalma-Navidad basins (Cecioni, 1983; Gonzalez, 1990; Encinas et al., 2006b). Offshore seismic profiles and focal mechanisms suggest that the forearc has been under compression during the Quaternary (Bohm et al., 2002; Geersen et al., 2011). The contractional inversion of normal faults in forearc basins along the south-central Andes has been associated with a shift from erosive to accretionary conditions during the Pliocene (Melnick and Echtler, 2006).

Rocky coasts and Holocene lowlands characterize the coastal geomorphology of the Maule rupture zone. The former are associated with resistant crystalline bedrock and are subjected to intense wave attack, whereas the latter occur mainly at the mouths of major rivers that carry predominantly volcanic detritus derived from the Andean volcanic arc (e.g. Mardones and Jaque, 1991). Northward-directed longshore drift further transports these sediments along the coast.

2.2. Quaternary crustal faults and previous estimates of coastal uplift rates

Quaternary faults have been described exclusively at the southern and northernmost sectors of the Maule rupture, namely the Lanalhue, Santa Maria and Pichilemu faults (Fig. 1B). The Lanalhue fault zone reactivates a Permian shear zone (Glodny et al., 2008) and bounds the southern Arauco Peninsula and Nahuelbuta Range, which form a major, ~100-km-wide, dome-like structure (Fig. 1B) (Rehak et al., 2008). Deformation patterns and the evolution of fluvial networks suggest domal uplift has been ongoing since the Late Pliocene and has been associated with the collision of a forearc sliver that extends to the south for ~1000 km (Melnick et al., 2009). The Santa Maria Fault system consists of a series of back-thrusts rooted in the interplate zone (Melnick et al., 2006), which generated surface ruptures during the Maule earthquake (Melnick et al., 2012b). The main Quaternary structures in the northern part of the Maule rupture zone are two NW–SE trending antiforms with associated normal faults at Pichilemu and Topocalma (Farías et al., 2011) (Fig. 1B). The Pichilemu normal fault generated two crustal M6.7 and M6.9 earthquakes 11 days after the Maule mainshock (Fig. 1A) and a cluster of aftershocks extending from the plate interface to almost the surface (Lange et al., 2012; Ryder et al., 2012).

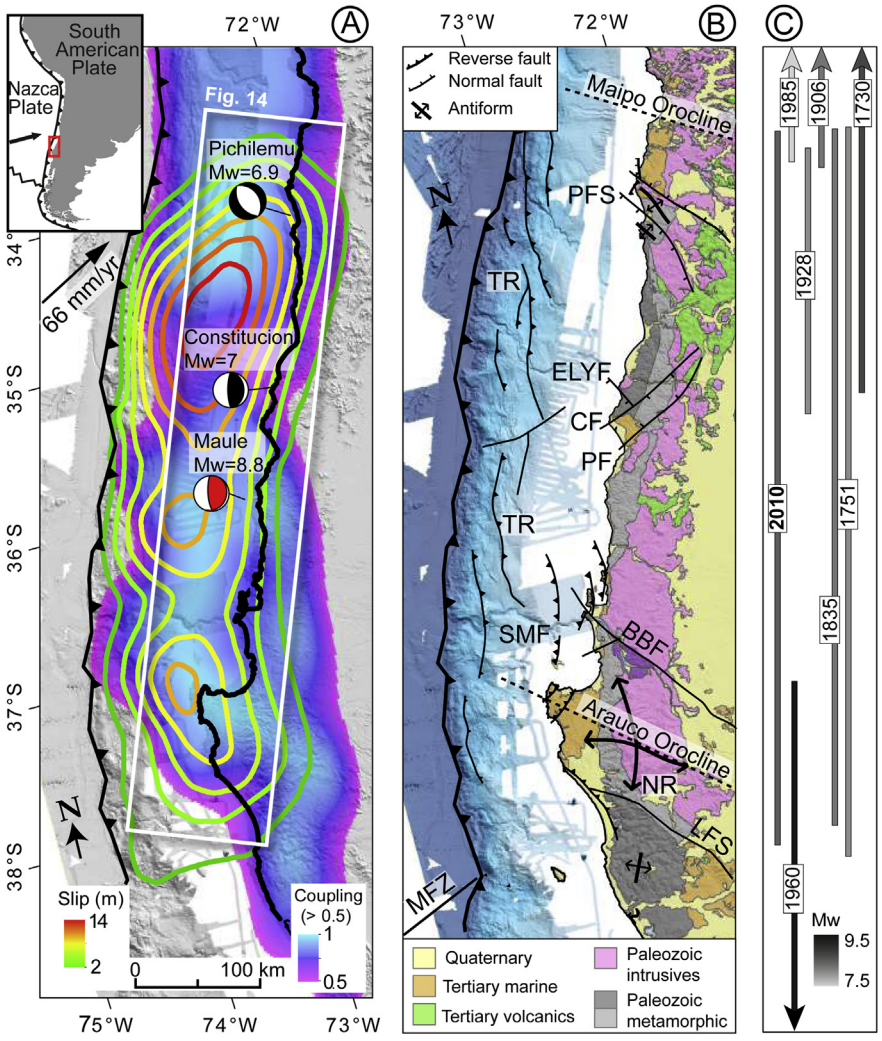

Fig. 1. Deformation patterns, historical earthquakes and regional geology along the 2010 Maule Earthquake rupture. (A) Co-seismic slip during the Maule earthquake (Moreno et al., 2012) and interseismic coupling before the event (Moreno et al., 2010). Slip contours every 2 m, red star represents the location of the epicenter (Vigny et al., 2011). The white rectangle indicates area of swath profiles in Fig. 14. Focal mechanism based on Farias et al. (2008), Vigny et al. (2011), Ruiz et al., 2013. (B) Geology and Quaternary structures. Black lines denote major upper plate faults. TR-thrust ridge, PFS-Pichilemu Fault System, SMF-Santa Maria Fault System, NR-Nahuelbuta Range, LFS-Lanalhue fault System, MFZ-Mocha Fracture Zone, BBF-Bio-Bio Fault, ELYF-El Yolki Fault, PF-Pelluhue Fault, CF-Carranza Fault. The black dashed lines indicate the symmetry axis of oroclines after Farías et al. (2008) and Melnick et al. (2009), (C) Rupture zone of historical earthquakes color-coded by estimated magnitude, see text for sources. (For interpretation of the references to color in this figure legend, the reader is referred to the web version of this article.)

Quaternary uplift rates along the coast have been obtained at only a few sites within the Maule rupture zone. Melnick et al. (2009) calculated a maximum uplift rate of 1.8 ± 0.2 m/ka using the ~125-ka-old marine terrace level at the Arauco Peninsula. North of Arauco Peninsula, at Santa Maria island, uplift rates between 1.8 ± 0.4 m/ka for the past ~50 ka (Melnick et al., 2006) and 2.1 ± 0.3 m/ka during the past ~4 ka (Bookhagen et al., 2006) were estimated. Farther south at Lanalhue Lake, Stefer et al. (2010) obtained a mean Holocene uplift rate of 0.42 ± 0.71 m/ka. Southwest of Arauco, at Mocha Island, Nelson and Manley (1992) determined uplift rates between 2 and 10 m/ka during the Holocene. At Algarrobo, Encinas et al. (2006a) calculated a Holocene uplift rate of 0.4 m/ka. These disparate estimates suggest large spatial variability in uplift rates along the Maule region.

2.3. Historical earthquakes in south-central Chile

Until 2010 the Maule area was considered to be a mature seismic gap in Chile (Barrientos, 1987; Campos et al., 2002; Ruegg et al., 2009). The historical earthquakes in the Maule segment include at least four well-documented megathrust events in 1730, 1751, 1835 and 1928 (Darwin, 1851; Campos et al., 2002; Lomnitz, 2004; Udías et al., 2012) (Fig. 1C) and the deeper intra-slab Chillan event of 1939 (Beck et al., 1998). The giant 1730 (M~9) event caused damage for a length of ~800 km along the coast with destructive tsunamis in Concepción and Valparaiso (Udías et al., 2012; Cisternas et al., 2014). Both the 1751 and 1835 events were great earthquakes very similar to the 2010 event and had estimated magnitudes of 8.5–8.8 (Udías et al., 2012). During the 20th century two further subduction events affected this region: the 1906 (M~8.6) earthquake, which overlapped about 200 km of the northern Maule rupture (Okal, 2005) and the 1928 (M~8.4) event that began near Constitución and ruptured to the north within the Maule segment (Lomnitz, 2004). The giant 1960 Valdivia (M9.5) earthquake, the largest recorded by modern seismology (Plafker and Savage, 1970; Cifuentes, 1989; Moreno et al., 2009), overlapped with the southern ~90 km of the Maule rupture across the Arauco

Peninsula. The 1985 (M8.0) Valparaiso earthquake (Barrientos, 1988) partly overlapped with the northern Maule rupture (Fig. 1C).

2.4. The 2010 Maule earthquake

The Maule earthquake of February 27 nucleated in the central part of its 500-km-long rupture zone and reached a moment magnitude of 8.8. This event corresponds to the sixth largest instrumentally recorded earthquake and the third largest in the era of space geodesy. Slip distributions for the Maule earthquake have been obtained by at least 12 studies using various methods and approaches (Delouis et al., 2010; Farias et al., 2010; Shao et al., 2010; Tong et al., 2010; Lorito et al., 2011; Pollitz et al., 2011; Pulido et al., 2011; Vigny et al., 2011; Moreno et al., 2012; Bedford et al., 2013; Lin et al., 2013; Yue et al., 2014). In spite of the differences among these model results, all the slip distributions derived from near-field geodetic data show a similar pattern formed by two main areas of high slip separated by a sector of reduced slip near the epicenter (e.g. Moreno et al., 2012; Lin et al., 2013) (Fig. 1A). The largest slip of more than 16 m occurred north of the epicenter in one major patch located mostly offshore (Moreno et al., 2012; Lin et al., 2013). The southern part of the rupture involved a secondary slip patch located mostly below the coastline with maximum slip of ~12 m. The down-dip termination of the rupture reached ~50 km depth (Tong et al., 2010; Moreno et al., 2012) coinciding at the surface with the trace of the coastline, except at the Arauco Peninsula where slip propagated farther inland. Kiser and Ishii (2011) suggested that slip in the northern part of the rupture dynamically triggered slip along the southern patch, both separated by a gap in rupture propagation, probably related to a mechanically weak zone.

Zones of coeval surface uplift and subsidence were recorded during the Maule earthquake, registered by GPS and field measurements using intertidal fauna (Farias et al., 2010; Vargas et al., 2011; Vigny et al., 2011; Jaramillo et al., 2012; Moreno et al., 2012; Melnick et al., 2012a). Slip in the northern offshore patch caused subsidence along the adjacent coastline while in the southern patch slip concentrated below the coastline resulting in coastal uplift. The maximum co-seismic uplift, estimated from measurements of intertidal fauna, was 2.5 m at Lebu and 2.4 m at Morguilla, both sites are located in the southwestern part of the Arauco Peninsula (Melnick et al., 2012a). Co-seismic coastal subsidence reached a maximum estimate of 0.5 m at Bucalemu, in the northern part of the rupture (Vargas et al., 2011). The hinge line between co-seismic uplift and subsidence was located at ~115 km from the trench (Fig. 2).

During the decade that preceded the Maule earthquake several studies attempted to quantify interseismic coupling along the Chile margin based on surface velocities estimated from GPS data (Klotz et al., 2001; Brooks et al., 2003; Khazaradze and Klotz, 2003; Moreno et al., 2008; Ruegg et al., 2009; Vigny et al., 2009). These studies suggested that interseismic coupling is characterized by lateral variations at scales of tens to hundreds of kilometers. Newer high-resolution and better-constrained models have revealed a heterogeneous distribution of interseismic coupling preceding the Maule earthquake (e.g. Moreno et al., 2010; Metois et al., 2012). The model of Moreno et al. (2010), which uses a detailed geometry of the megathrust based on Tassara et al. (2006), shows two highly coupled patches (>90%) separated by a region of reduced coupling

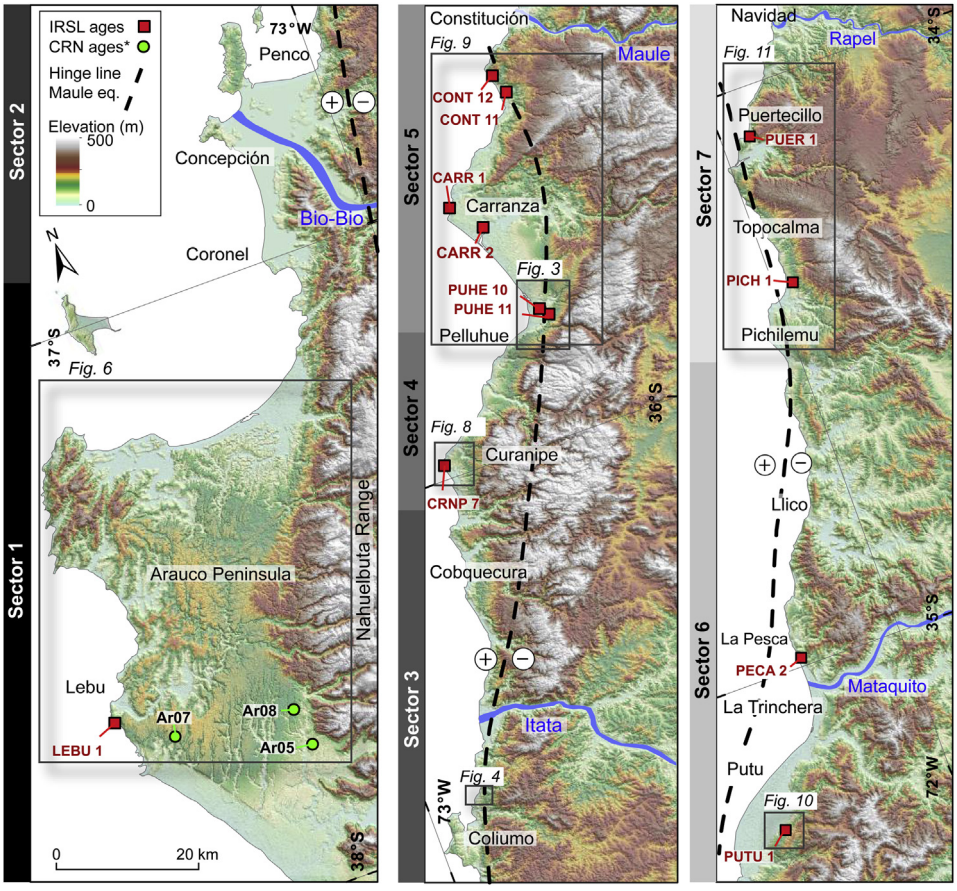

Fig. 2. Shaded-relief map showing sampling locations for age dating and the 7 sectors with characteristic terrace patterns described in text. The hinge line of co-seismic land-level change is indicated by the dashed line with the respective sense of motion. Figure locations are indicated with black boxes.

(50–70%) at the center of the rupture (Fig. 1A). According to Moreno et al. (2012) these coupled patches are roughly coincident, but not blueprint copies of the co-seismic slip distribution during the Maule earthquake (Fig. 1A). In this study we use the inter- and co-seismic models of Moreno et al. (2010) and (2012), respectively, because these authors adopted the same modeling strategy as well as detailed geometries of the plate interface and lithosphere constraints by geophysical data, the largest number of GPS stations as well as InSAR and coastal land-level change data.

In an attempt to characterize the mechanism of segmentation of the Maule earthquake rupture different approaches have been used. For instance, Aron et al. (2013) suggested that faults with suitable orientation with respect to the co-seismic slip are likely to be active during the co-seismic phase segmenting the rupture zone. At the southern boundary of the rupture, Lin et al. (2013) inferred that a velocity-weakening patch just below the Arauco Peninsula might facilitate the propagation of dynamic ruptures into the area but not through it, probably due to its large size (~100 km). At the northern part of the rupture, Farías et al. (2011) suggested that lithological heterogeneities locally increase the normal stresses on the megathrust causing a permanent barrier that has stopped earthquake propagation throughout the Quaternary. In the search for a tectonic control of earthquake segmentation, Moreno et al. (2012) noticed that the pattern of co-seismic slip correlates with inflections in the curvature of the slab, which may produce variations in shear stresses on the megathrust, also affecting the dynamic propagation of the rupture. The proposed correlation between long-term tectonic features and patterns of co-seismic deformation implies that the Maule segment has probably been sustained over longer timescales, although, the northern limit of the Maule rupture was certainly breached by the 1730 earthquake (Fig. 1C; Udías et al. (2012)).

3. Background and methods

3.1. Marine terraces as geomorphic markers of permanent deformation

Marine terraces are geomorphic markers that may provide relevant information about coastal paleo-dynamics and vertical tectonic movements (e.g. Dupré, 1984; Trenhaile, 2002; Marquardt et al., 2004; Saillard et al., 2009; Limber and Murray, 2011). Marine terraces are formed by the interaction between eustatic sea-level fluctuations and tectonic uplift (Bradley, 1957; Lajoie, 1986; Muhs et al., 1990; Anderson et al., 1999); during episodes of sea-level rise and during highstand periods a wave-cut platform is carved into the landscape whenever wave erosion forces cliff retreat (Anderson et al., 1999). The wave-cut platform may be abandoned during the next low-stand period, leaving behind a terrace deposit or veneer of marine and continental sediments (Bradley, 1957). If the uplift rate is fast enough the platform can be preserved during the next highstand period at higher elevations and remain unaffected by rising sea level. An emerged marine terrace is thus preserved, while a new platform will be sculpted at lower elevation (e.g. Rosenbloom and Anderson, 1994). Considering that presently sea-level is at the highest position since the Marine Isotope Stage (MIS) 5e (Shackleton et al., 2003; Hearty et al., 2007), marine terraces formed during or after the MIS 5 that are still recognizable in the landscape are generally preserved as a result of rapid tectonic uplift (Lajoie, 1986; Pedoja et al., 2011).

Wave-cut marine terraces consist of smooth planar surfaces with slope angles between 1 and 15° that may be covered by a thin veneer of sediments (Merritts et al., 1991; Anderson et al., 1999; Bowles and Cowgill, 2012). Geomorphic features such as seastacks, landslides and gullies can locally increase the roughness of marine terraces (Scott and Pinter, 2003). Some authors have used the terrace tread directly as a proxy for terrace elevation (e.g. Scott and Pinter, 2003; Bowles and Cowgill, 2012) although uplift rates estimated from such markers will be systematically underestimated. The terrace tread is usually bounded inland by a paleo-cliff and characterized by the shoreline angle located where the paleo-cliff intersects the tread. The shoreline angle has been considered as the best horizontal datum of past sea-level positions (e.g. Bradley and Griggs, 1976; Lajoie, 1986; Ashby et al., 1987; Scott and Pinter, 2003). The elevation of the shoreline angle has been directly correlated with sea-level highstands (Eq. (1)) providing a measure to estimate the net vertical displacement and associated uplift rate of a particular terrace level (e.g. Berryman et al., 1989; Weber, 1990). Nevertheless, uplift rates that include a correction for eustatic sea level might be biased by the uncertainties in the chosen sea-level curve (e.g. Pedoja et al., 2011; Yildirim et al., 2013).

In contrast to wave-cut terraces, constructional or wave-built terraces are gently sloping landforms formed by thick piles of sediments transported either along the coastline or across the wave-cut platform (Gilbert, 1890; Jackson et al., 2005). The sedimentary cover of wave-built terraces records transgressive–regressive cycles associated with repeated terrace reoccupation episodes, commonly resulting in a flat composite surface devoid of clear geomorphic indicators of past sea-level positions. We therefore used the stratigraphic information to infer past sea-level positions as described in Jara-Muñoz and Melnick (2015).

Marine terraces are ephemeral landforms which start to be degraded by fluvial and hillslope processes immediately after their abandonment (Anderson et al., 1999). For instance, terrace treads and cliffs tend to be dismantled by river incision, while the shoreline angle is often obscured by eolian and colluvial deposits. In order to unmask the original terrace morphology, we developed a new method based on the analysis of the maximum elevation extracted from swath profiles.

3.2. Mapping marine terraces

Geologic field mapping focused on identifying the type of terrace surface, location of paleo-cliffs, bedrock lithology, and the stratigraphy and thickness of associated sedimentary deposits. This information was used to help correlating isolated terrace levels. To increase the precision of our analysis we used bare-earth digital elevation models derived from LiDAR point clouds filtered and interpolated at 0.5 and 2.5 m grid size for selected sites (Fig. 3A and DR1). Additional sites were analyzed using contour maps at 2 and 5 m spacing from Chilean governmental sources (further details in Section DR1). Contours were interpolated using the Topo-to-Raster tool in ArcGis® to create hydrologically-corrected digital elevation models (DEMs).

To identify and map terrace surfaces we used the surface classification model (SCM) (Fig. 3A) of Bowles and Cowgill (2012). The SCM linearly combines the terrain roughness and slope, highlighting the extent of low-relief and smooth surfaces. SCM maps facilitate the identification of different terrace levels, their extent and distribution of elevations (Fig. 3B). However, SCM maps by themselves cannot be used directly to determine the shoreline angle elevation, which requires a profile-based analysis.

3.3. Estimating shoreline angle elevations

The accurate assessment of terrace elevation is essential to obtain reliable uplift rates. One of the major problems when

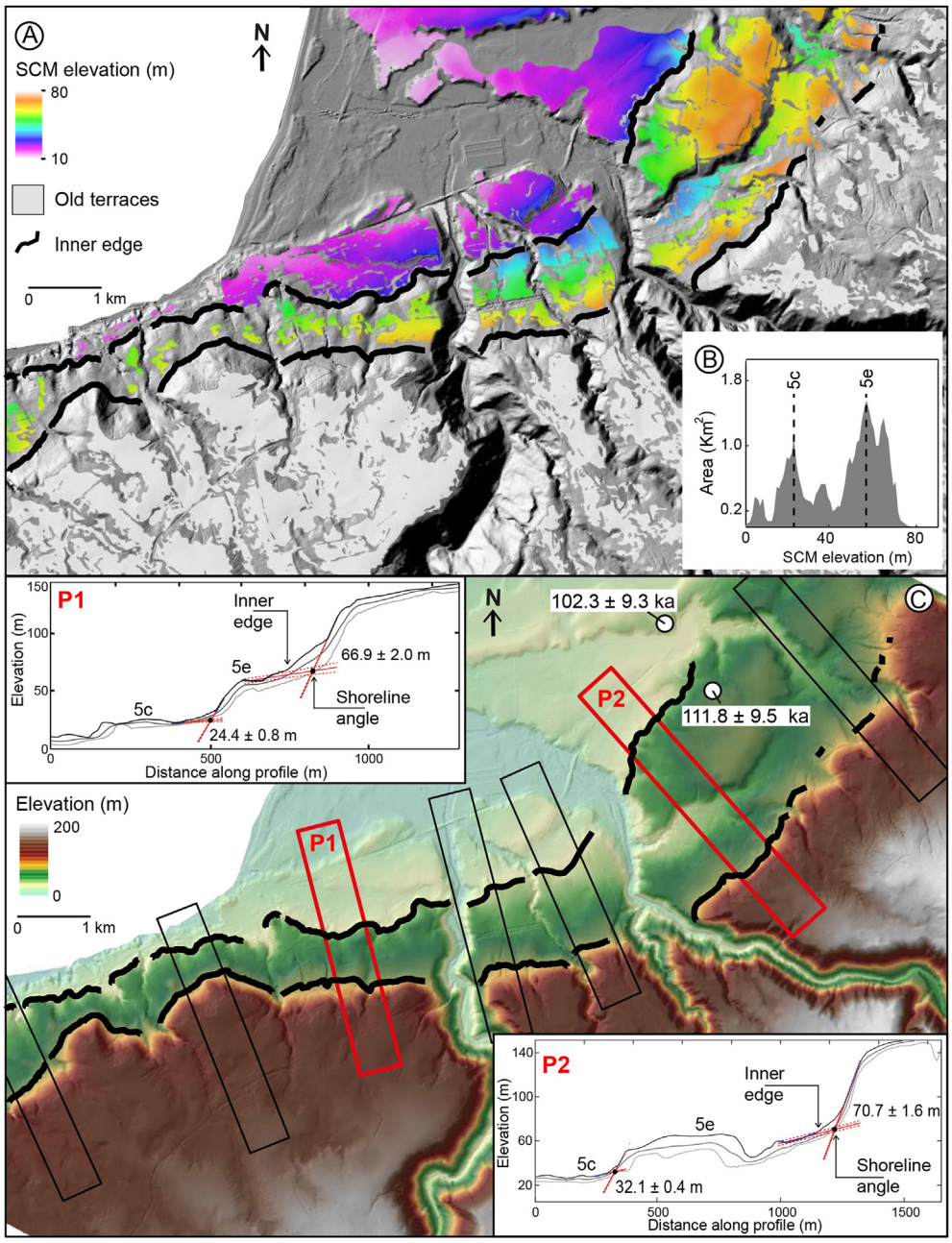

Fig. 3. Example of mapping and analysis of marine terraces at Pelluhue (Sector 4). (A) Shaded LiDAR relief with color-coded elevation of the surface classification model used for automated mapping of terrace levels, after Bowles and Cowgill (2012). (B) Histogram of elevations obtained from classified areas. Note peaks at the two distinct terrace levels. (C) 2.5-m LiDAR DTM with inner edges of MIS 5c and 5e terrace levels denoted by thick black lines. Rectangles indicate location of swath profiles analyzed using TerraceM (see text for details). Insets show two examples of the analysis (P1 and P2) highlighting the position of shoreline angles and inner edge of the two terrace levels deduced by extrapolation of the paleo-cliff and abrasion platform with 2σ errors. (For interpretation of the references to colour in this figure legend, the reader is referred to the web version of this article.)

estimating the elevation of the shoreline angle of Pleistocene marine terraces is the presence of colluvial wedges obscuring the original cliff morphology (Hanks et al., 1984). Direct measurements of terrace elevations using the foot of the paleo-cliff (or terrace inner edge) commonly result in an overestimation of the uplift rate; this bias will be greater in regions of low uplift rate.

To precisely measure the elevation of shoreline angles in wave-cut terraces we developed TerraceM, a graphical user interface in MATLAB®. This algorithm uses the maximum elevation extracted from swath profiles (Figs. 3C and 4), in order to avoid the effects of fluvial overprints. Points representing the undisturbed abrasion platform and paleo-cliff are picked and fitted by linear regression. Both linear fits are extrapolated and intersected to determine the elevation of the buried shoreline angle. The associated error is based on the linear regressions of both the abrasion platform and the paleo-cliff at the 95% confidence interval (2σ) (Fig. 3C).

Rough coasts are analyzed by extrapolating the top of sea stacks to the cliff locating the shoreline angle. We detected peaks from the maximum elevation of swath profiles using an automated algorithm based on spectral analysis and feature recognition (Fig. 4). Peaks were separated according to elevation classes and linearly interpolated to reconstruct the paleo-topography of the eroded platform, and the elevation of the shoreline angle was estimated from the intersection of the extrapolated linear fit and the cliff. The error estimates of the shoreline angle elevation are based on the

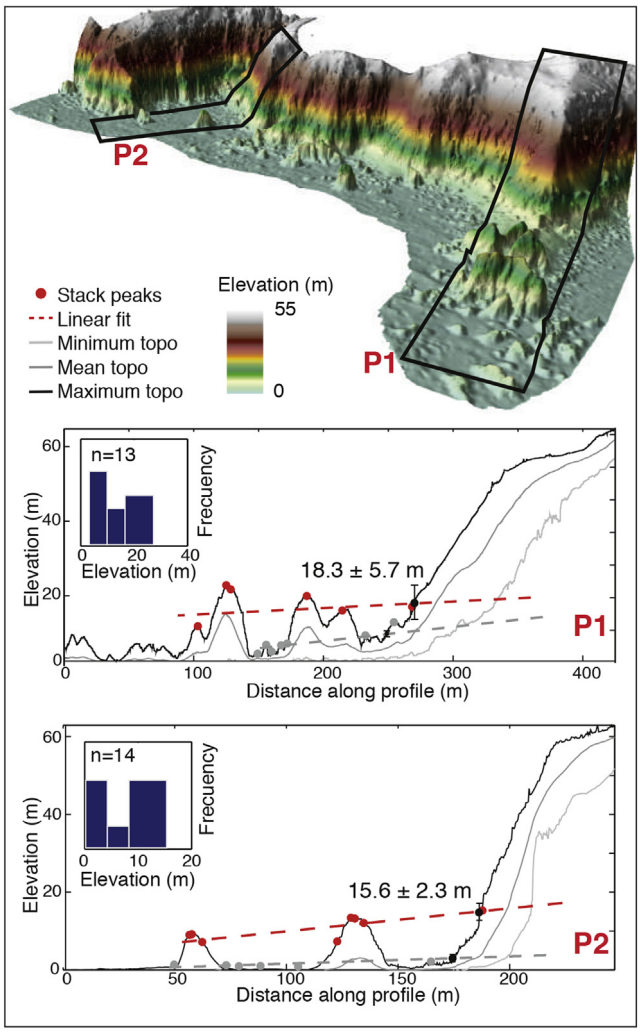

Fig. 4. Example illustrating the methodology used at rough coasts. Perspective view of 0.5-m LiDAR DTM at Coliumo (Sector 3). Two swath profiles (P1 and P2) were analyzed by peak detection from the maximum elevation envelope isolating the position of sea-stack (red dots) and allowing reconstructing the paleo-abrasion platform by linear interpolation back to the sea cliff. The position of the shoreline angle is found at the intersection of the paleo-abrasion platform with the cliff. Errors are 2σ. (For interpretation of the references to color in this figure legend, the reader is referred to the web version of this article.)

extrapolation of linear regressions of peak populations at a 95% confidence interval (2σ) (Fig. 4).

3.4. Stratigraphy and luminescence dating of marine terrace deposits

Sediments covering marine terraces can be used to approximate their minimum age (e.g. Muhs, 2002; Zazo et al., 2003; Zecchin et al., 2009; Bianca et al., 2011; Gurrola et al., 2014). Terrace deposits commonly consist of regressive sequences deposited in high-energy nearshore environments immediately after a sea-level highstand; their stratigraphy is controlled by the local relative sea level and coastal dynamics (e.g. Bradley, 1957; Dupré, 1984). Depending on the supply of sediments and the number of involved sedimentary cycles, these deposits can generate wave-built terraces. In this study, we analyze the stratigraphy of MIS 5 terraces to assist in spatial correlations among disparate sites. We infer the depositional environment and determine the number of sedimentary cycles. The stratigraphic sections were described according to different facies including sedimentary structures, mineralogy, and grain-size distribution, with particular emphasis on characterizing flooding surfaces.

Twelve sediment samples from terrace deposits were dated using the post-IR Infrared stimulated luminescence (IRSL) signal of K-feldspar. Samples consisted of sandy sediments, either of eolian or beach berm depositional environments, and were collected at depths between 1.8 and 4.5 m below the surface (Table 1; Fig. DR3). Given that quartz is known to generate unstable luminescence signals for some Andean sediments (e.g. Steffen et al., 2009), we used exclusively coarse grains of K-Feldspar (100–250 μm) measured according to the $pIRIR_{290}$ SAR protocol (See Section DR2 for more details). The suitability of the terrace samples for luminescence dating was indicated by high feldspar signals with adequate reproducibility; dose recovery tests after signal resetting in a solar simulator for 12 h resulted in acceptable ratios between measured and laboratory dose (0.9–1.1) for all samples. Burial doses were calculated on the basis of 14–19 accepted aliquots, with a diameter of 8 mm, using the central age model (CAM) of Galbraith et al. (1999), and corrected for residual doses afterwards (Fig. 5B and C). In addition, the completeness of signal resetting (bleaching) was evaluated on the basis of a present-day sample from a beach berm (sample SM mb, Table 1).

Radionuclide analysis (uranium, thorium and potassium) for dose-rate estimation was carried out using high-resolution gamma-spectrometry to estimate the dose rate. Attenuation of radiation by pore water was considered by using measured water contents between 5 ± 5 and 16 ± 5 weight-%. Sampling depth, geographical position and altitude above sea level were used to calculate the contribution of cosmic radiation (Prescott and Hutton, 1994). For estimation of internal dose rates, a potassium content of 12.5 ± 0.5% was adopted (Huntley and Baril, 1997).

3.5. Estimating uplift rates from shoreline angle elevations and luminescence ages

Eustatic sea-level variations during MIS 5 have been well documented worldwide (e.g. Kukla et al., 2002; Muhs, 2002; Shackleton et al., 2003; Hearty et al., 2007). MIS 5 is divided into three highstand periods between 80 and 135 ka (Shackleton et al., 2003; Dumas et al., 2006). Most studies have concluded that sea-level was approximately 5 m above its present-day elevation during MIS 5e (Hearty et al., 2007; Pedoja et al., 2011, 2014), and 20 m below during both MIS 5a and 5c (Potter et al., 2004; Rohling et al., 2009). In order to correlate our IRSL ages with their corresponding MIS stage we used the sea-level curve of Rohling et al. (2009) (Fig. 5A), which is the most recent high-resolution sea-level curve for the southern hemisphere, spanning the last 550 ka. Uplift rates have been estimated using the relation: (Lajoie, 1986)

$$u = (E - e)/T \quad (1)$$

We first calculate the relative sea-level position (H) based on the difference between the terrace elevation (E) and sea-level position at the time of terrace formation (e). By dividing the relative sea-level by the age of the terrace level (T) we obtained the uplift rate (u). The standard error (Se(u)) is calculated using the following relation: (Gallen et al., 2014)

$$Se(u)^2 = u^2\left(\left(\sigma^2 H / H^2\right) + \left(\sigma^2 T / T^2\right)\right) \quad (2)$$

where σH is the error in relative sea-level:

$$\sigma H = \mathrm{sqrt}(\sigma E^2 + \sigma e^2) \quad (3)$$

Table 1
Infrared stimulated luminescence (IRSL) ages.

Sample code	Long	Lat	Elevation (m)	Sample depth (m)	Palaeodose (Gy)	Aliquot size (mm)	Number of aliquots	RSD (%)	OD (%)	U (ppm)	Th (ppm)	K %	Water content (%)	Age (ka)
PUTU 1	−72.25	−35.16	79	2.4	123.3 ± 8.2	8	13	17	15.4	0.8 ± 0.04	2.69 ± 0.16	0.39 ± 0.01	13	84.7 ± 7.6
PUHE 11	−72.54	−35.8	45	3.6	212.4 ± 12.2	8	12	11.2	8.98	1.05 ± 0.05	4.24 ± 0.25	0.78 ± 0.03	16	111.8 ± 9.5
PUHE 10	−72.55	−35.8	35	1.8	194.0 ± 12.9	8	12	16.02	14.8	1.12 ± 0.06	4.72 ± 0.27	0.68 ± 0.03	16	102.3 ± 9.3
CONT 11	−72.47	−35.44	72	4.5	229.5 ± 14.2	8	11	13.4	11.7	0.86 ± 0.04	3.5 ± 0.20	0.81 ± 0.03	15	124.1 ± 10.8
PICH 1	−71.97	−34.38	51	2.8	242.1 ± 13.5	8	5	7.16	1.98	1.44 ± 0.07	4.94 ± 0.28	0.86 ± 0.03	5	106.1 ± 9.3
CONT 12	−72.49	−35.4	21	4.3	220.1 ± 14.1	8	18	18.4	16.4	1.30 ± 0.07	5.05 ± 0.29	1.07 ± 0.04	17.8	104.7 ± 7.8
PUER 1	−71.94	−34.09	50	1.7	231.8 ± 13.44	8	17	11.7	11.3	1.18 ± 0.06	3.94 ± 0.24	1.40 ± 0.05	4.6	87.3 ± 6.9
PECA 2	−72.18	−34.98	20	4.2	572.6 ± 53.5	8	17	35.07	31.8	1.48 ± 0.08	7.37 ± 0.42	1.57 ± 0.06	9.5	192.9 ± 20.1
CARR 1	−72.61	−35.58	30	3.8	157.6 ± 11.7	8	19	26.1	23.4	1.32 ± 0.07	5.02 ± 0.29	1.30 ± 0.05	7.7	67 ± 5.7
LEBU 1	−73.67	−37.62	100	1.4	157.7 ± 13.9	8	18	31.1	29.9	1.01 ± 0.05	3.96 ± 0.23	0.53 ± 0.02	20.1	89.2 ± 9.4
CARR 2	−72.54	−35.64	33	2.8	240.6 ± 16.2	8	19	20.8	19.5	1.32 ± 0.07	4.84 ± 0.28	1.15 ± 0.04	14.7	103.5 ± 9
CRNP 7	−72.78	−35.97	17	1.8	485.9 ± 41.6	8	19	30.06	29.8	0.68 ± 0.05	4.24 ± 0.31	0.74 ± 0.04	16.6	265 ± 28.5
SM mb[a]	−73.51	−37.04	2	0.5	3.4 ± 0.1	8	15	9.7	8.5	–	–	–	3.6	1.5 ± 0.09

RSD = relative standard deviation, OD = overdispersion, U = uranium, Th = thorium, K = potassium.
[a] Modern beach berm sample.

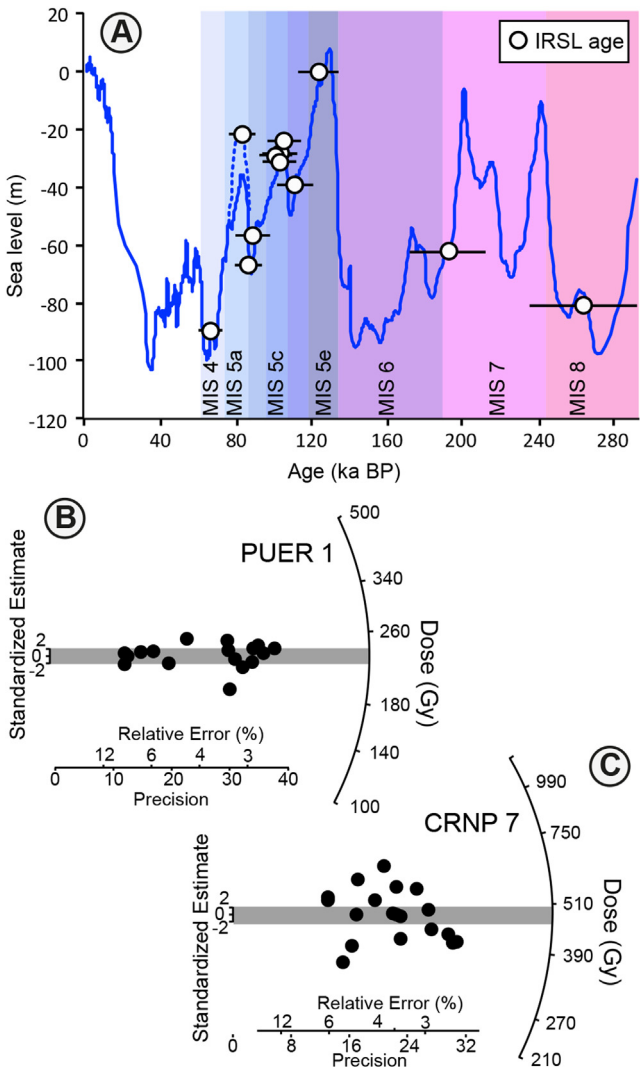

Fig. 5. Luminescence dating results. (A) Global sea-level curve of Rohling et al. (2009) with IRSL ages (2σ errors) plotted at their corresponding paleo sea-level position, the sea-level during MIS 5a is based on (Potter et al., 2004) and indicated by dashed lines. (B and C) Radial plots of equivalent dose data of samples PUER 1 and CRNP 7. Note scattering in dose distribution for sample CRNP 7. (See section 4.1.4). Further information and plots of IRSL results can be found in the Data Repository.

Standard error estimates include the 5-m uncertainty in absolute sea level (σe) (Rohling et al., 2009), error estimates of the shoreline angle elevations (σE), and an arbitrary range of 5 ka for the duration of the highstands (σT). The highstand duration has been inferred from the mean ranges of MIS 5e lasting from 130 to 119 ka Hearty et al. (2007) and MIS 5c from 107 to 98 ka (Potter et al., 2004; Rohling et al., 2009).

Before applying Eq. (1), we first corrected the ages and elevation of terrace surfaces depending on their type (Table 2). For instance, for wave-cut terraces or for terraces covered by a thin sedimentary veneer, we correlate the terrace age with the nearest older sea-level highstand; finally, to calculate the uplift rate we use both, the shoreline angle elevation and the corrected age of the terrace. For wave-built terraces, based on the ages obtained within the sedimentary sequence we follow the method proposed by Jara-Muñoz and Melnick (2015) approximating the age of the bedrock unconformity with the preceding highstand. Then, we use the bedrock elevation and its corrected age to calculate the vertical displacement rate. This is based on the following assumptions: a) terrace veneer formation starts immediately after the highstand (Dupré, 1984); b) the age of the bedrock discontinuity is coeval with the onset of deposition; and c) The cumulative wave energy necessary to carve the bedrock abrasion platform can only occur during a protracted period of time, mostly during highstands (Anderson et al., 1999).

4. Results

4.1. Geomorphology, stratigraphy and luminescence ages of marine terraces

Marine terraces are broadly distributed along the Maule coast. Based on the distribution of their geomorphic characteristics, ages, geology, and elevation patterns, we subdivided the 2010 rupture zone into seven sectors described below from south to north as labeled in Fig. 2. The sedimentary sequences associated with marine terraces along the Maule rupture have been used to correlate the age of the terrace surfaces. These sequences have a clear mineralogical signature depending on their age. The nature of sedimentary sequences, their geomorphic setting, their ages, and correlations with highstands are described below and are illustrated in Figs. 6–12 (further details in Section DR3).

4.1.1. Sector 1: Arauco Peninsula – Coronel

The Arauco Peninsula is located in front of the Nahuelbuta Range, the highest region of the Coastal Range within the Maule

Table 2
IRSL and CRN age calibrations with geomorphic and stratigraphic markers and their corresponding highstand.

Sample code	Sector	Sample elevation (m)	Age (ka)	MIS	Sea-level[b] (m)	Apparent uplift rate[c] (m/ka)	Marker elevation (m)	Type of marker	Assigned age[d] (ka)	Assigned MIS	Sea-level (m)[e]	Corrected uplift rate (m/ka)
PICH 1	7	51	106.1 ± 9.3	5c	−23.4	0.70	60 ± 0.4	SA	106 ± 5	5c	−20	0.75 ± 0.06
PUER 1	7	50	87.3 ± 6.9	5b	−66.24	1.33	75.91 ± 4.6	SA	106 ± 5	5c	−20	0.90 ± 0.08
PUTU 1	6	79	84.7 ± 7.6	5a	−20	1.16	32.7 ± 3	BU	106 ± 5	5c	−20	0.50 ± 0.06
PECA 2	6	20	192.9 ± 20.1	7	−62.19	0.43	15 ± 1.0	BU	200 ± 5	7	−5	0.10 ± 0.03
CONT 11	5	72	124.1 ± 10.8	5e	0.21	0.58	72 ± 1.0	SA	125 ± 5	5e	5	0.54 ± 0.05
CONT 12	5	21	104.7 ±7.8	5c	−28.3	0.50	38.9 ± 0.2	SA	106 ± 5	5c	−20	0.56 ± 0.05
CARR 1	5	30	67 ± 5.7	4	−89.03	1.78	44 ± 5.0	SA	84 ± 5	5a	−20	0.76 ± 0.1
CARR 2	5	33	103.5 ± 9	5d	−30.9	0.62	53 ± 5.0	SA	125 ± 5	5e	5	0.38 ± 0.06
PUHE 11	4	45	111.8 ± 9.5	5d	−38.7	0.75	71.3 ± 1.8	SA	125 ± 5	5e	5	0.53 ± 0.05
PUHE 10	4	35	102.3 ± 9.3	5c	−28.3	0.62	33 ± 0.5.0	SA	106 ± 5	5c	−20	0.50 ± 0.05
CRNP 7	3	17	265 ± 28.5	7	−80	0.37	17 ± 1.0	BU	125 ± 5	5e	5	0.10 ± 0.04
LEBU 1	1	100	89.2 ± 9.4	5b	−56.3	1.75	120.72 ± 5.6	SA	106 ± 5	5c	−20	1.33 ± 0.09
Ar08[a]	1	50	130 ± 14	5e	−1	0.39	142.69 ± 6.1	SA	125 ± 5	5e	5	1.10 ± 0.08
Ar08[a]	1	50	133 ± 14	5e	−28	0.59	142.69 ± 6.1	SA	125 ± 5	5e	5	1.10 ± 0.08
Ar05[a]	1	61	130 ± 13	5e	−1	0.48	107.55 ± 5.7	SA	125 ± 5	5e	5	0.82 ± 0.07
Ar07[a]	1	150	127 ± 13	5e	4	1.15	142.69 ± 6.1	SA	125 ± 5	5e	5	1.10 ± 0.08

SA = shoreline angle, BU = bedrock unconformity.
[a] CRN samples from Melnick et al. (2009).
[b] Sea-level based on Potter et al. (2004) and Rohling et al. (2009).
[c] Apparent uplift obtained directly from sample age and elevation.
[d] Assigned nearest last highstand age.
[e] Sea-level at assigned highstand.

rupture with maximum elevations reaching 1500 m (Fig. 2). Marine terraces assigned to MIS 5e in this area were collectively named the Cañete surface by Kaizuka et al. (1973) and dated to between 127 and 133 ka (MIS 5e) by Melnick et al. (2009) with cosmogenic nuclide exposure dating using ^{10}Be and ^{26}Al. The terrace morphology consists of a wide eastward tilted erosion surface (Fig. 6A) covered by near-shore deposits that increase in thickness towards the north and south (Fig. 6C and D). The shoreline angles are located at a maximum distance of ~30 km inland from the present-day coastline. The terraces are warped along a northwest-southeast–oriented uplift axis reaching a maximum elevation of 200 m at the central part of the peninsula (Fig. 6B).

Sequences of coastal sediments defined as the Cañete Formation (MIS 5e) are associated with the Cañete surface along the Arauco Peninsula (Fig. 6C). The thickness of these deposits increases from a minimum of 20 m at the central part of the peninsula to 50 m in the northern part (Fig. 6D). At its base the Cañete Formation comprises horizontally and cross-stratified black volcanic sandstone overlain by massive medium sandstone with insect burrows, fine lamination and paleosols.

At Lebu, in the southwestern edge of the Arauco Peninsula, a lower terrace level with a shoreline angle elevation at 122 ± 1 m is located 1.4 km inland from the coastline (Fig. 6A). This terrace is sculpted into Tertiary sedimentary bedrock and covered by nearshore marine and eolian deposits (Fig. DR7). This up to 8-m-thick sequence consists of black volcanic sandstone and conglomerate, and can be divided into two units, each representing a distinct sedimentary cycle separated by a 40-cm-thick paleosol horizon. The lower level is formed by a matrix-supported polymictic and well-rounded conglomerate that grades upward into medium sandstone. The upper unit consists of massive and horizontally stratified coarse to medium black volcanic sandstone. An IRSL age obtained from the eolian unit yielded 89.2 ± 9.4 ka suggesting this terrace level was formed during MIS 5c. Thus, the first unit was likely associated with transgressive deposition synchronous with a sea-level rise episode during MIS 5c, whereas the second unit appears to have been associated with a sea-level fall followed by eolian deposition during MIS 5b.

4.1.2. Sector 2: Coronel – Penco

MIS 5e terraces are well preserved and decrease in elevation northward (Fig. 12A, Fig. DR8). The terraces are sculpted into metamorphic rocks and are covered by a ~10-m-thick veneer of eolian and shallow marine siliceous sandstone in the southern part of this sector. No ages could be obtained from siliceous sediments due to the absence of feldspars; however, terrace surfaces in this area are virtually continuous toward the south with those of Sector 1 across the Arauco Peninsula. A ~15-km-wide zone of upwarping identified at Coronel is likely associated with local faulting (Fig. 12B). Shoreline angle elevations of the MIS 5e level increase northward from 51 to 83 m immediately south of the Bio–Bio River. MIS 5e terrace elevations decrease abruptly across the Bio–Bio down to 6.3 ± 0.6 m at Penco, the lowest elevation along the Maule rupture. This abrupt change in terrace elevation is also likely associated with the local influence of the Bio–Bio Fault (Fig. 12B).

4.1.3. Sector 3: Penco – Curanipe

In the southern part of this sector the coastline is rough, rocky and narrow, enclosed by 30- to 70-m-high sea cliffs with only small pocket beaches. Marine terraces from MIS 5e in this sector are narrow and discontinuous, sculpted into intrusive and metamorphic rocks, and located adjacent to the present-day rocky coastline. The MIS 5e level is partially destroyed by ongoing wave erosion forming sea stacks and stumps (Fig. 7C) as well as isolated narrow wave-cut terraces. Stacks form where portions of a retreating coast become isolated through erosion and dissection of the cliff base (e.g. Trenhaile et al., 1998); these features are detached from the cliff forming columns, stack-arcs and caves (Fig. 7B). The base of these features is usually submerged whereas the tops are distributed at similar elevations thus suggesting they represent fragments of an eroded terrace level. We analyzed the elevation of these terrace remnants using the peak detection method (Fig. 4) obtaining shoreline angle elevations that increase northward from 9 to 48 m (Fig. 12A).

At Cobquecura, we identified an older well-defined terrace level located ~1 km inland from the coastline and at ~80 m elevation covered by a veneer of layered arkose (Fig. DR9). This terrace level is

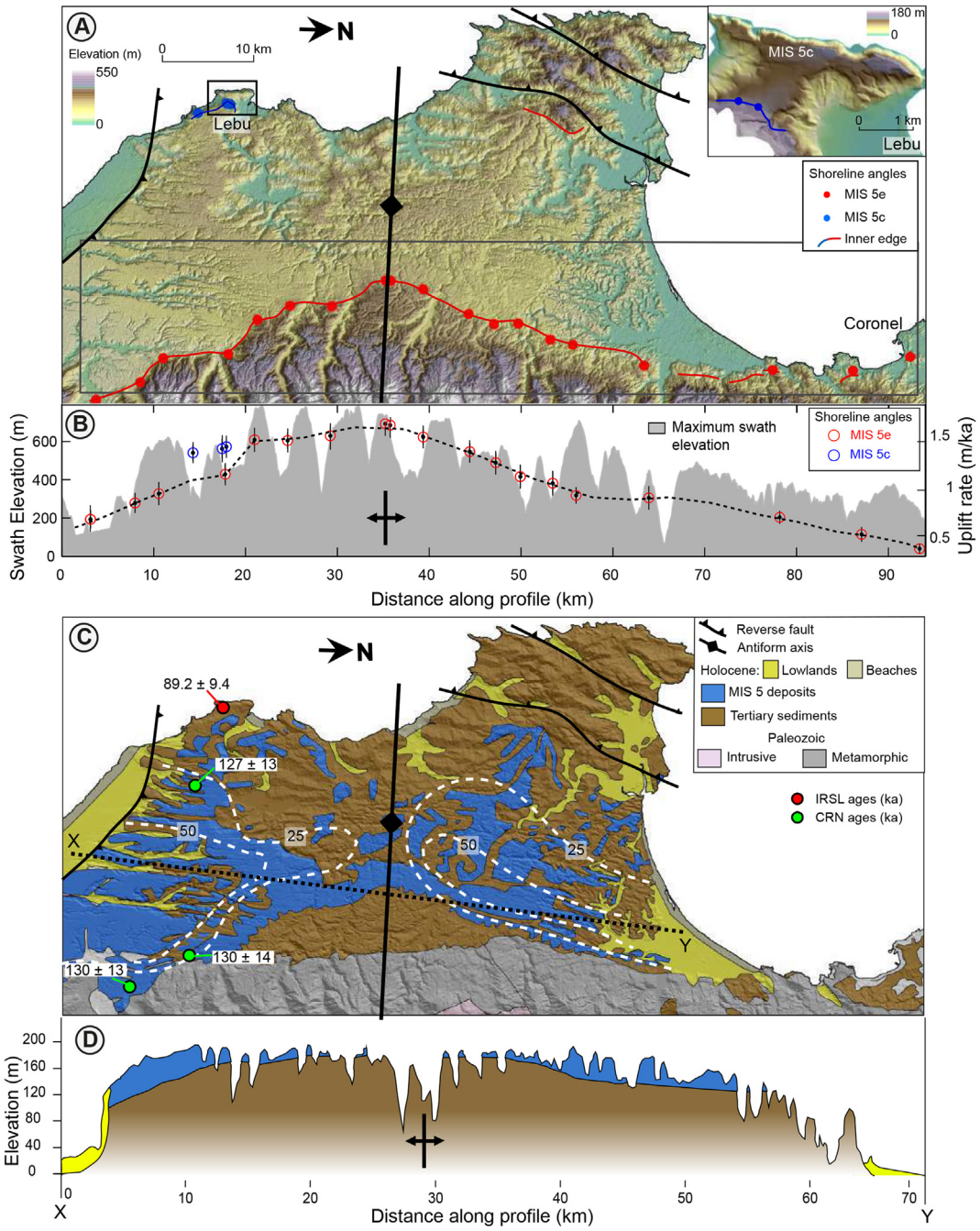

Fig. 6. Marine terraces and geology of the Arauco Peninsula. (A) Distribution of MIS 5 shorelines and main Quaternary structures in the Arauco Peninsula. Inset shows distribution of MIS 5c terraces at Lebu on a 2-m DEM, black rectangle indicates location of swath profile in B. (B) Profile showing uplift rates for MIS 5e and MIS 5c terraces above topographic swath profile. (C) Simplified geologic map. White dashed line indicates isopach contours of MIS 5e deposits from Melnick et al. (2009). (D) Geologic profile highlighting the axis of the Arauco anticline and increase in sediment thickness of MIS 5e sequences suggesting syntectonic deposition. The axis coincides with the maximum elevation of MIS 5e shorelines.

older than MIS 5 and was not considered in the morphometric analysis, but the distinct stratigraphic and the mineralogic signature of the arkosic deposits could be found at several locations and thus helped to infer the position of pre-MIS 5 levels (Fig. DR10).

4.1.4. Sector 4: Curanipe – Pelluhue

Two distinct terrace levels with continuous geomorphic expression could be clearly differentiated in this area and correlated along the coast for more that 30 km. Wave-cut terraces are exposed with narrow treads north of Curanipe changing to staircase morphology at Pelluhue. Based on two IRSL ages obtained at Pelluhue of 111.8 ± 9.5 and 102.3 ± 9.3 ka, we correlated these levels with MIS 5e and MIS 5c, respectively (Figs. 3A and 7F). At Pelluhue the MIS 5 paleo-coast follows the shape of the bay forming a well-exposed flight of marine terraces. Terraces are partly covered by elongated littoral bars that progressively widen northwards partly obscuring the paleo-cliff morphologies (Figs. 3A and 9A). Terrace elevations in this area increase locally northward defining a small-scale flexure where the MIS 5e level reaches a maximum elevation of 75 m (Fig. 12A).

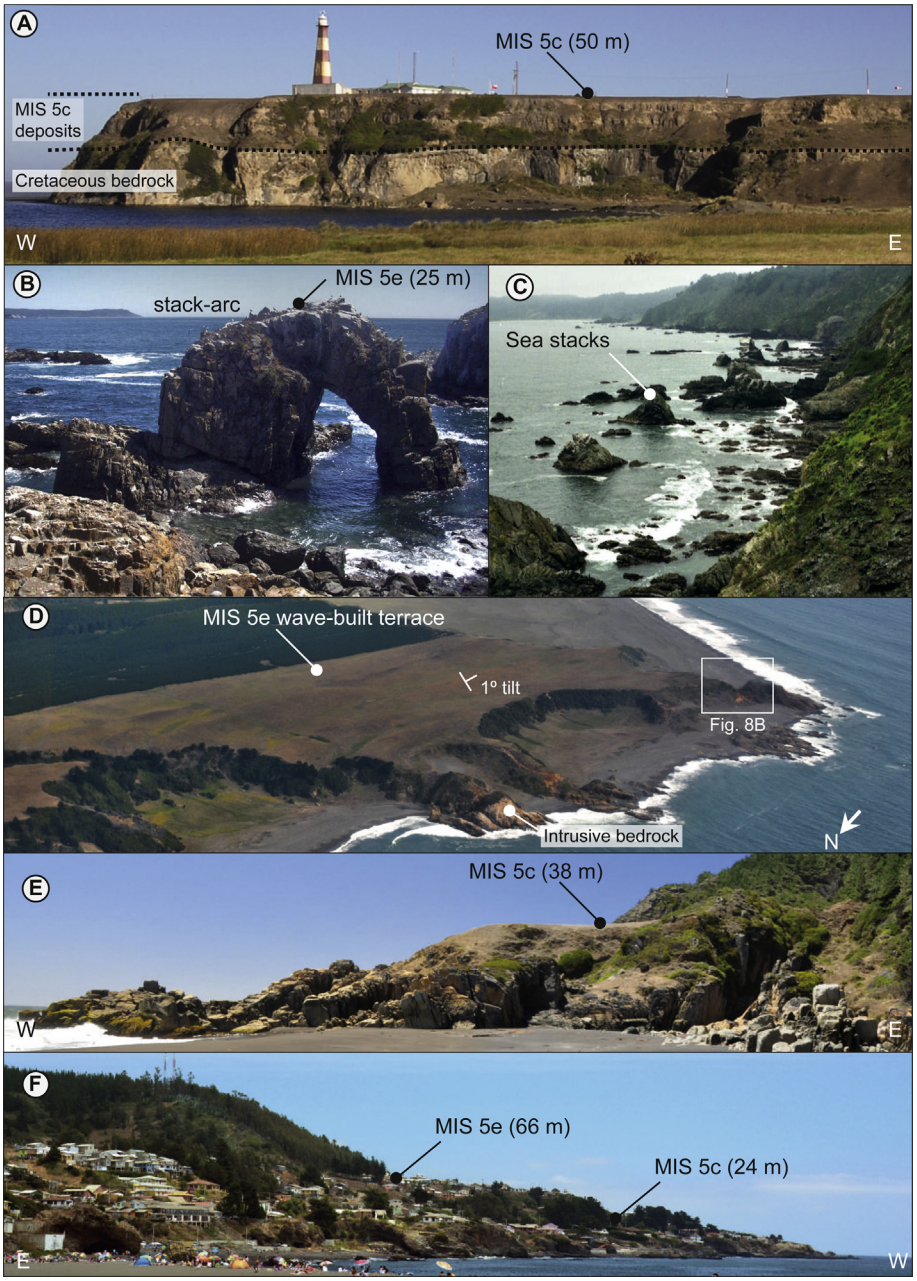

Fig. 7. Field views showing the geomorphic expression of MIS 5 terraces. (A) Prominent terrace level at Carranza (Sector 5). Deposits consist of eolian sandstones deposited above Cretaceous bedrock. (B, C) Geomorphic features of rough coasts including stack-arcs and clustered sea stacks at Coliumo (Sector 3). (D) Oblique aerial view of a wave-built terrace at Curanipe. Terrace surface is tilted 1° southward, see detailed map and LiDAR DTM in Fig. DR7. (E) Example of a sharp wave-cut terrace north of El Yolki (Sector 5) correlated with MIS 5c. (F) Example of a staircase terrace sequence at Pelluhue (Sector 4).

A wave-built terrace with a wedge-like geometry is exposed at Curanipe and onlaps the intrusive bedrock (Fig. 8D and E). The absence of clear paleo-cliff morphologies prevented the estimation of a shoreline angle. Nevertheless, we could measure a ~1° southward tilt of the terrace surface, which follows the elevation change of the MIS 5 terrace levels (Fig. 7D). The Curanipe sedimentary sequence is divided into a lower unit predominantly formed by arkose with fine layers of magnetic minerals (Fig. 8C) and an upper unit consisting of black stratified volcanic sandstone, separated by a ~2-m-thick paleosol (Fig. 8A). The upper unit consists of massive and cross-stratified eolian sandstone with lenticular paleosol intercalations and horizontally bedded volcanic sandstone. The upper unit is pervasively affected by post-depositional precipitation of iron oxide in convolute crusts as well as disseminated in the matrix. An IRSL age of 265 ± 28.5 ka was obtained from black sandstone at the base of the upper unit (Fig. 8B).

Black volcanic sandstone is almost exclusively found in the MIS 5 deposits, which in turn are devoid of arkosic lithologies. Arkosic sediments characterize MIS 7 and possibly older deposits found in Sectors 3, 4 and 6. Therefore the apparent MIS 7 age obtained from black sandstone of the upper unit at Curanipe (Fig. 8A) is inconsistent with the characteristic regional mineralogical signatures. No direct connection exists between the Main Cordillera and this sector of the coast that could have locally transported volcanic material during MIS 7.

Alternatively, we infer that pervasive post-depositional precipitation of iron at this site might have affected the luminescence age. Potential effects of mineral precipitation on luminescence dating

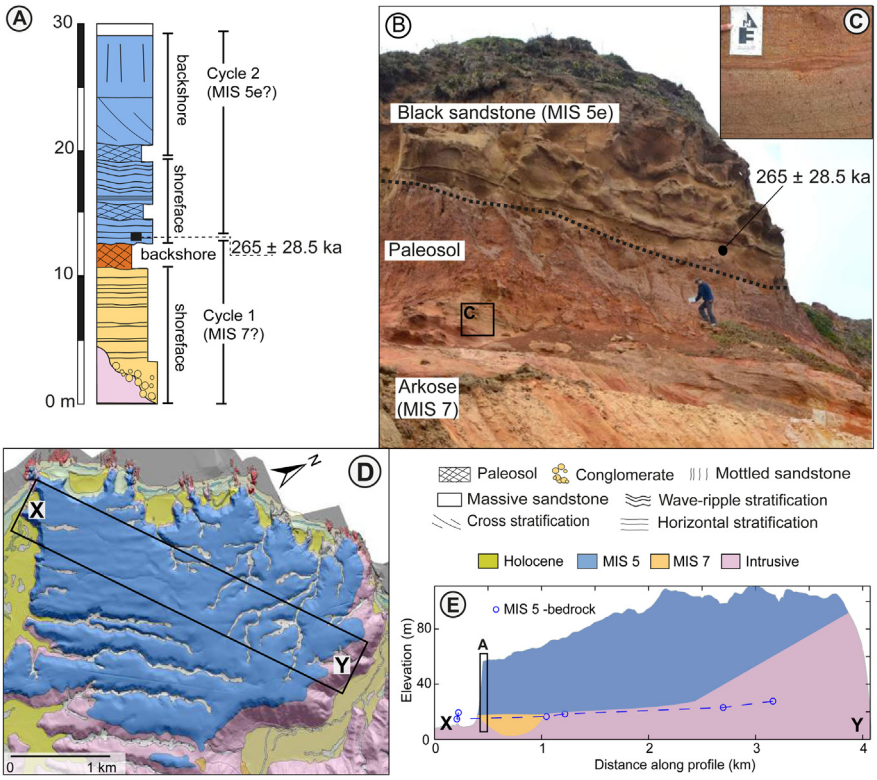

Fig. 8. Wave-built marine terrace at Curanipe (Sector 3), (A) Stratigraphic section showing the two sedimentary units consist of horizontally stratified black to brownish volcanic sandstone correlated with MIS 5. (B) Field view of the sedimentary sequence. (C) Detail view of the finely laminated arkose correlated with MIS 7 (see text for details). (D) Geologic map superposed on LiDAR shaded relief indicating the extent of the black sandstone unit correlated with the MIS 5e. (E) The sequences represent a sedimentary body onlapping the intrusive bedrock.

have been inferred to dilute radioelements (U, Th) and thus lower the dose rate (e.g. Mauz, 1999). Such effects would have an effect on dosimetry, changes in porosity and thus water contents as well as radiogenic element concentrations. Although effects on dose rates (in form of temporal variations) are hard to detect, comparably high values of dose scatter can be observed in the dated sample at Curanipe (CRNP 7) (34% over dispersion compared to ~20% in most other samples; Fig. 5B and C). These high values could result from spatially inhomogeneous dosimetry due to radiation hotspots at iron concentrations affecting the final age results as well. Considering the potential inaccurate age estimate of this sample and based on the mineralogical signature, we tentatively correlate the upper unit at Curanipe with the MIS 5e level.

4.1.5. Sector 5: Pelluhue-Constitución

In the southern part of this sector (between Pelluhue and Carranza) the terraces are partly covered by Pleistocene sediments and active dunes, making the measurement of shoreline angles difficult. The morphology is characterized by a ~5-km-wide smooth surface that increases in elevation progressively towards the southeast. At Pelluhue MIS 5 sediments form two stacked sequences comprising massive black volcanic sandstone with horizontal and cross stratification dated as 102.3 ± 9.3 ka and 111.8 ± 9.5 ka, respectively. Given that each sequence represents a distinct sedimentary cycle and the obtained ages are coincident with distinct sea-level highstands, we correlate the two terraces surfaces with MIS 5c and 5e.

At Carranza terrace levels consist of a wave-cut platform sculpted into Cretaceous sediments forming a broad surface covered by Pleistocene deposits (Fig. 9A). These strata consist of a sequence of almost exclusively massive black volcanic sandstone deposited in an eolian environment and of fluvial deposits found on relict fluvial terraces along the main drainages. An age of 67 ± 5.7 ka was obtained from eolian deposits, suggesting deposition during the MIS 4. We infer that these eolian deposits cover a poorly preserved terrace inner edge south of Carranza that probably was formed during MIS 5c. This is supported by the presence of dated MIS 5c marine sediments at the southern and northern parts of this sector. Fluvial deposits yielded an age of 103.5 ± 9 ka (MIS 5d), suggesting relict terraces formed during MIS 5e.

At the northern part of Sector 5 (El Yolki) two distinct terrace levels could be identified at ~40 and ~80 m. Sediments associated with these levels consist of black marine and eolian sandstone that can be divided in two stacked sequences deposited on the metamorphic basement and above an older unit of white siliceous sandstone (Fig. 9C and DR11). Both sequences are formed by a transition from shoreface to backshore deposits, each representing a distinct sedimentary cycle. Based on IRSL ages of 124.1 ± 10.8 and 104.75 ± 7.8 ka obtained for each sequence, we correlate them with MIS 5e and 5c stages, respectively (Fig. 9C and DR11).

4.1.6. Sector 6: Constitución – Pichilemu

An up to ~7-km-wide Holocene coastal plain with a field of active dunes extending for ~40 km from Putu to La Trinchera characterizes this sector (Fig. 2). These lowlands are bounded by a ~60-m-high steep paleo-cliff limiting the MIS 5 terraces at Putu. In this sector the elevation of MIS 5 terraces decreases northward and their surface expression becomes discontinuous.

A wave-built terrace crops out at Putu (Fig. 10A and C). The sequence consists of stratified black volcanic sandstone divided in three units that represent two sedimentary cycles (Fig. 10B). The lower unit consists of horizontally laminated sandstone with magnetic minerals, representing upper shoreface sedimentation

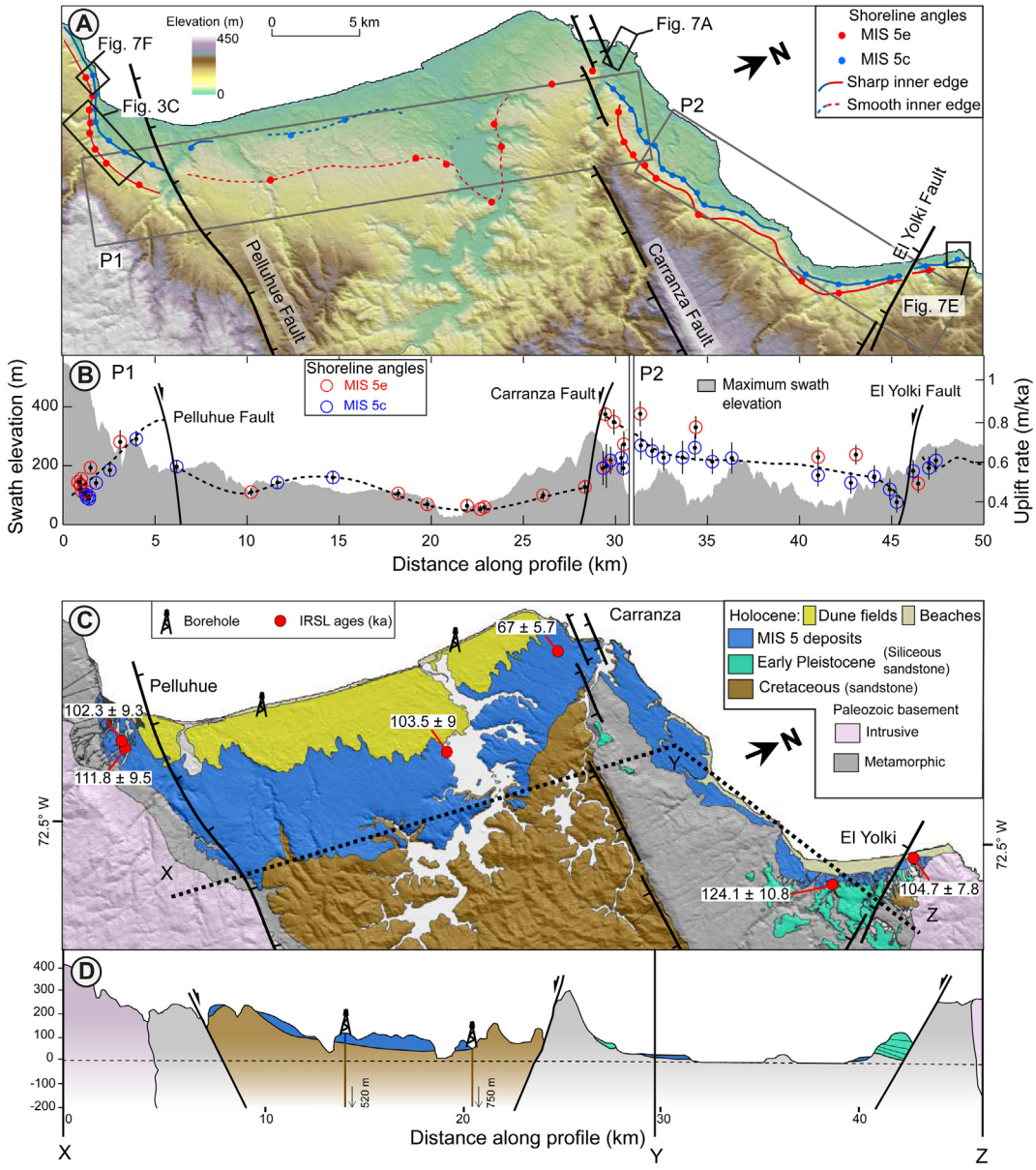

Fig. 9. Marine terraces and geology at Carranza. (A) Map of MIS 5 shorelines and Quaternary faults. Black rectangles (P1 and P2) indicate location of swath profiles in B. Note the sharp scarp associated with the normal faults. (B) Uplift rates estimated from MIS 5e and MIS 5c shorelines and topographic swath profile. (C) Geologic map and IRSL ages of MIS 5 deposits. (D) Geologic profile showing relation between crustal faults and the geometry and thickness of Cretaceous and Pleistocene deposits filling a central graben, originally inferred from hydrocarbon exploration boreholes (Cecioni, 1983).

above a wave-cut platform (Fig. 10D). This unit is overlain by cross-stratified massive sandstone interbedded with clay lenses that represent backshore deposits. The upper unit is formed by horizontally stratified coarse to medium sandstone deposited in an upper shoreface environment overlain by massive and cross-stratified sandstone deposited in a backshore environment (Fig. 10B). The upper unit is correlated with MIS 5a based on an age of 84.7 ± 7.6 ka. We correlated the two lower units with a regressive episode during MIS 5b immediately after formation of the wave-cut platform during MIS 5c.

A pronounced terrace level defined as La Trinchera by Araya-Vergara (1976) occurs at ~200 m elevation in the central part of Sector 6 and extends northwards (Fig. 2 and DR13). This wave-built terrace consists of a ~70-m-thick sequence of arkose and sandstone with lithic fragments, and at least four distinct interbedded paleosol horizons. We obtained an age of 205.6 ± 22.3 ka near the base of the sequence confirming that the arkosic sediments are older than MIS 5 (Fig. DR13). The geomorphic markers of this terrace were not considered in our analysis, which was restricted to MIS 5 levels. A preserved terrace remnant was identified in the northern part of Sector 6 at the outlet of the Llico River, where it forms a fluvio-marine terrace partly covered by active dunes (Fig. DR12). We tentatively correlate this level with MIS 5e based on its position below an older level formed by arkosic sediments. The tentative MIS 5e shoreline angle is at an elevation of ~15 m.

4.1.7. Sector 7: Pichilemu – Navidad

Terraces in this sector were sculpted into the metamorphic basement and Tertiary marine deposits of the Navidad Formation (Encinas et al., 2006b), and are covered by black marine and eolian

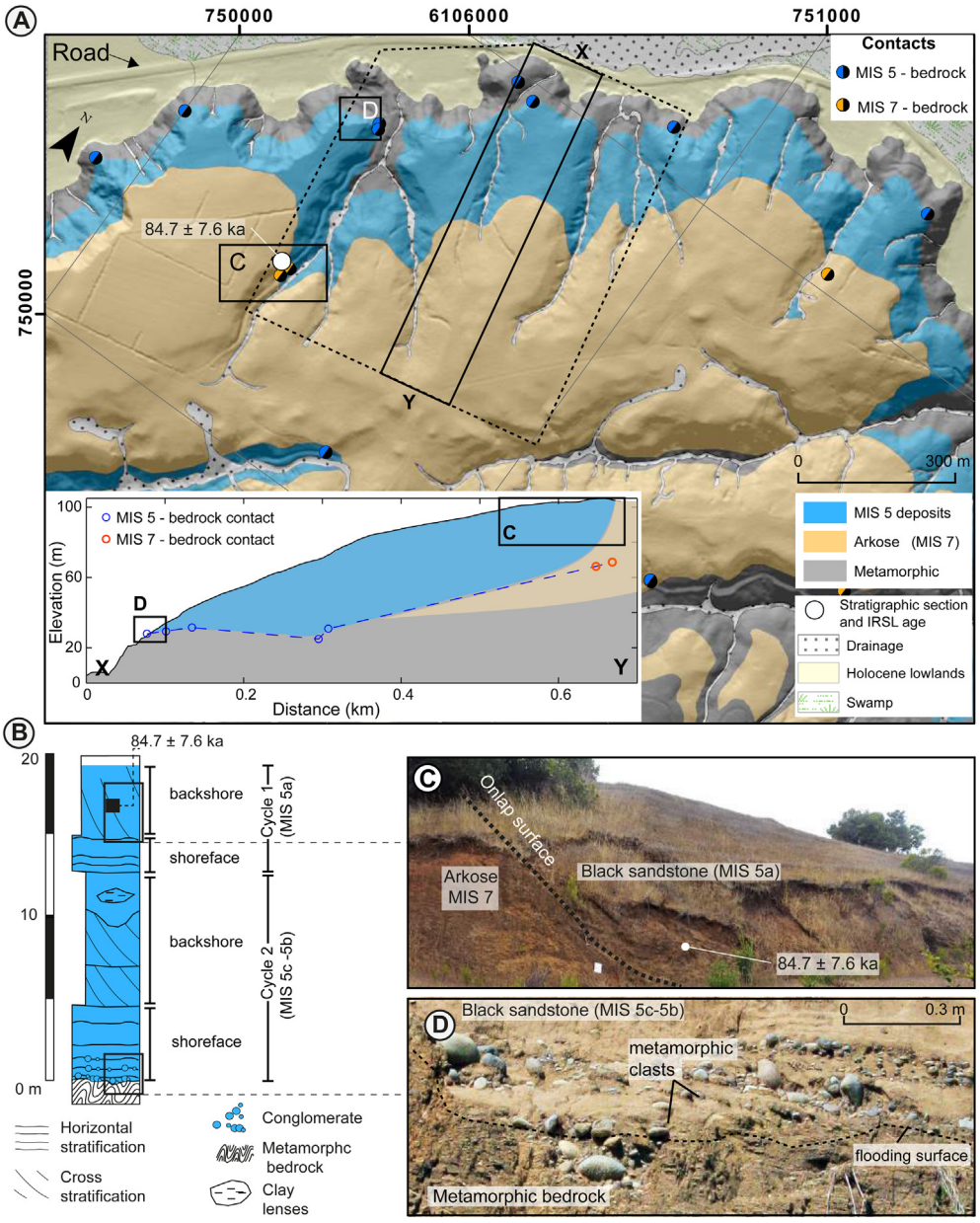

Fig. 10. Geology and stratigraphy at Putu. (A) Geology superposed on LiDAR shaded relief map. The site consists of black volcanic sandstone deposited above the metamorphic bedrock and arkosic sequences. Inset shows a geologic profile highlighting the wedge-shaped geometry of the wave-built terrace and measurement points. (B) Stratigraphic section showing the two sedimentary cycles. (C) Field view showing the onlap between the MIS 5c back sandstone and the MIS 7 arkosic unit. (D) View of the basal conglomerate that characterize the flooding surface.

sandstones, which decrease in thickness northward (Fig. 11C). Marine terraces are offset across the Pichilemu Fault and at Topocalma these surfaces display a broad warping pattern with elevations increasing from 40 to 180 m (Fig. 11B). At Puertecillo, a normal fault deforms the sedimentary sequences and offsets the MIS 5e level from ~180 to ~150 m; the fault-line scarp of another N–S–striking normal fault has been reoccupied by the MIS 5c and 5e sea-cliffs (Fig. DR15).

MIS 5c deposits at Pichilemu comprise mostly stratified black volcanic sandstone (Fig. DR14). The terrace deposits consist of two units that represent a sedimentary cycle deposited above a wave-cut platform sculpted into metamorphic rocks. The lower unit consists of horizontally stratified sandstone, representing upper-shoreface deposits, and the upper unit constitutes cross-stratified and massive sandstone, deposited in eolian environment. An age of 106.1 ± 9.3 ka obtained from the lower unit suggests deposition during MIS 5c. The northernmost outcrops of MIS 5 deposits occur at Puertecillo (Fig. DR15), where they form a sedimentary body laterally attached to the bedrock. The sequence was dated at 88.2 ± 6.9 ka (MIS 5b) and consists of massive and cross-stratified black volcanic sandstones deposited in an eolian environment. Considering that eolian deposits represent the ultimate phase of sedimentation, immediately after a sea-level fall episode, we correlate the age of this terrace surface with MIS 5c.

In the northern part of Sector 7 terrace elevations become progressively lower and discontinuous. At Navidad we correlated terrace remnants at an elevation of 17 m with MIS 5e. This level is absent farther north where the coast is characterized by plunging cliffs sculpted into Tertiary rocks suggesting rather stable tectonic conditions.

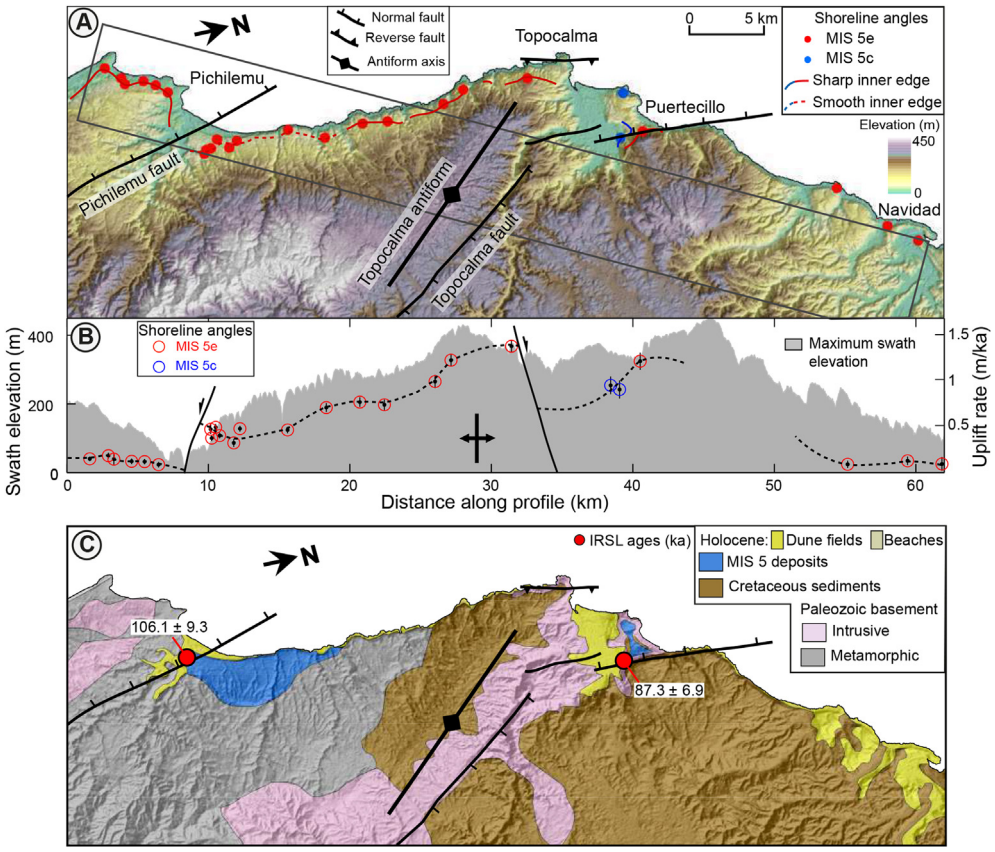

Fig. 11. Marine terraces and geology between Pichilemu and Topocalma. (A) Map showing the distribution of MIS 5 inner edges and Quaternary structures, the black rectangle indicates location of swath profile in B. (B) Profile showing uplift rates estimated from MIS 5e and MIS 5c shoreline angles and topographic swath profile. Note offsets associated with the Topocalma and Pichilemu faults. (C) Simplified geologic map modified from Farías et al. (2011) and references therein showing IRSL ages from MIS 5 levels.

4.2. Distribution of Quaternary faults and uplift rates along the Maule rupture

We were able to estimate uplift rates for 170 elevation measurements of shoreline angles from MIS 5c and 5e terrace levels (Fig. 12, details in Section DR4). Uplift rates of marine terraces along the Maule rupture have a mean of 0.5 m/ka (estimated from a 5-km linear interpolation to avoid spatial bias). Importantly, this mean rate is exceeded at Arauco, Carranza and Topocalma, where uplift rates reach maximum values of 1.59, 0.85, and 1.35 m/ka, respectively. In turn, the areas between these three sectors are characterized by relatively low uplift rates between 0.1 and 0.2 m/ka (Fig. 12B).

Interestingly, the fastest uplifting regions, Arauco and Topocalma, are both located at the boundaries of the Maule rupture and are characterized by wide antiformal structures with wavelengths of 90 and 60 km, respectively. The Arauco antiform is delineated by an increase in elevations of MIS 5e shoreline angles, the maximum elevation of the topography, and a decrease in thickness of MIS 5e deposits toward the center of the peninsula (Fig. 6). These opposite variations in thickness and shoreline elevation are consistent with coeval growth of the antiform (Melnick et al., 2009). The Topocalma antiform is delineated by an increase in elevation of both MIS 5c and 5e terraces and in maximum topography (Fig. 11). The Topocalma antiform is bounded by two NW-SE-striking normal faults at Pichilemu and Puertecillo, which offset the terraces by ~30 m with an associated minimum vertical displacement rate of ~0.5 m/ka (Fig. 12B and DR15). The distribution of shoreline angle elevations, mimicking the topographic expression of the Topocalma antiform, is consistent with an NW–SE oriented uplift axis (Fig. 11A). This structure apparently extends across the entire Coastal Range (Farías et al., 2011).

The region of moderately fast uplift (0.85 m/ka) at Carranza is located in the central part of the Maule rupture and disrupted by the Pelluhue, Carranza, and El Yolki faults (Fig. 9B and D). These extensional structures locally offset and fold the MIS 5 terraces along a 45-km-long stretch of coast. The Carranza Fault is associated with an NE-striking and SE-facing steep topographic break and together with the Pelluhue Fault juxtaposes Cretaceous sedimentary rocks with the metamorphic basement forming a symmetric graben (Fig. 9D). Both structures control the local drainage pattern formed by a drowned valley in the central part of the graben and perched paleo-surfaces in the uplifted footwall block of the Carranza Fault (Fig. 9A).

Immediately north of Carranza the MIS 5c terrace is well exposed forming a ~2-km-wide platform at elevations that rise from ~40 to ~100 m and then decrease gently northward back to ~40 m at the hanging wall of the El Yolki Fault, another hitherto unrecognized Quaternary structure (Fig. 9B). This scissor-type normal fault dips to the southwest and progressively increases in throw towards the northwest, forming a small halfgraben filled with Pleistocene siliceous sandstone (Fig. 9D and DR11). The fault consists of several segments arranged in a left-stepping en échelon geometry suggesting a minor left-lateral horizontal component. The MIS 5e level is offset by ~25 m and the MIS 5c level by ~10 m across the El Yolki Fault. The MIS 5e terrace level is displaced vertically ~23 and ~50 m across the Pelluhue and Carranza faults,

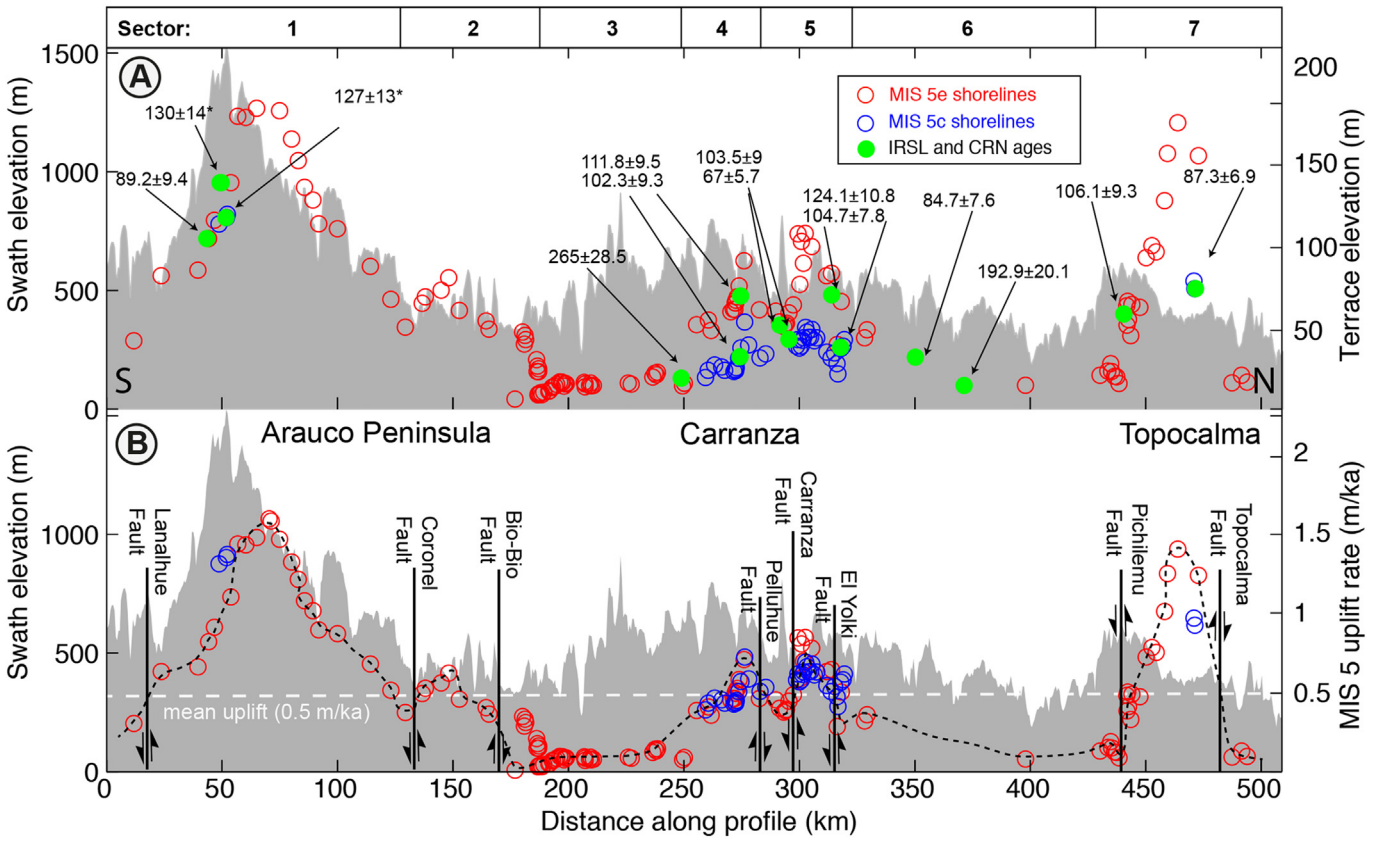

Fig. 12. Permanent deformation patterns along the Maule rupture. (A) MIS 5 terrace elevations, ages and maximum swath topography. (B) Uplift rates deduced from MIS 5 terraces, main faults and maximum swath topography. White dashed line indicates the mean uplift rate.

respectively. Based on these offsets we estimated minimum vertical displacement rates of ~0.2 m/ka for the Pelluhue and El Yolki faults, and ~0.4 m/ka for the Carranza Fault.

5. Discussion

5.1. Uplift mechanisms responsible for emerged marine terraces

Our detailed assessment of variable uplift rates estimated from marine terraces along the Maule earthquake rupture reveals that permanent deformation is distributed heterogeneously along strike, probably reflecting the segmentation of the forearc into discrete blocks. The central part of the rupture zone at Carranza is characterized by moderate uplift rates, sharp fault offsets, and short-wavelength flexures related to footwall back-tilting and rollover monoclinal folding. In turn, the boundaries of the Maule rupture are characterized by broad zones of crustal upwarping associated with the highest uplift rates. The origin of long-wavelength structures has been related with deep-seated sources (e.g. Melosh and Raefsky, 1980; Watts and Daly, 1981), which along the Maule segment are possibly related to changes in the mechanical behavior of the megathrust and/or the entire crust.

Interestingly, Arauco and Topocalma are both located at the shortest distances from the trench of 75 and 90 km, respectively, and both spatially correlate with well-known morphotectonic features of the entire Andean orogen. For instance, Topocalma is located immediately south of the Maipo Orocline (Farías et al., 2008), interpreted to result from the collision of the Juan Fernández Ridge with the continental margin since ~10 Ma. Analogously, the Arauco Peninsula is located at the symmetry axis of the Arauco Orocline (Fig. 1B), associated with the northward motion of a forearc sliver that extends for 1000 km southward resulting in margin-parallel shortening (Melnick et al., 2009). Along-strike changes in the margin-parallel dip (curvature) of the plate interface also occur at the position of these oroclines (Fig. DR16), emphasizing the profound changes in the geometry of the entire margin across these two zones.

Hypothetically, the geometry of the plate interface could control the pattern of long-term permanent deformation, generating long-wavelength structures above curved segments (e.g.Bonnardot et al., 2008). To test this hypothesis we compared uplift rates with distance to the trench, slab depth, and the margin-parallel component of slab dip (Fig. 13C–E and DR16). Arauco and Topocalma show an inverse relationship between distance-to-trench and uplift rate (Fig. 13A), suggesting areas closer to the trench rise faster. Conversely, these parameters are not correlated at Carranza. Topocalma and Arauco also show a wide range of uplift rates at shallower plate interface depths with respect to Carranza (Fig. 13D), suggesting areas where the slab is shallower may uplift faster. An interesting relationship emerges when the margin-parallel slab dip is compared with the uplift rate. Carranza is correlated with a concave-upward portion of the plate interface whereas Arauco and Topocalma are associated with convex to planar sectors (Fig. 13E).

We infer that the curvature and depth of the plate interface may control the distribution of uplift rates and extent of long-wavelength structures that are ultimately associated with boundaries of subduction-zone earthquakes. Changes in slab curvature may facilitate local underplating and basal accretion of subducting trench sediments forming duplex structures that could account for the generation of the long-wavelength zones of upwarping (Glodny

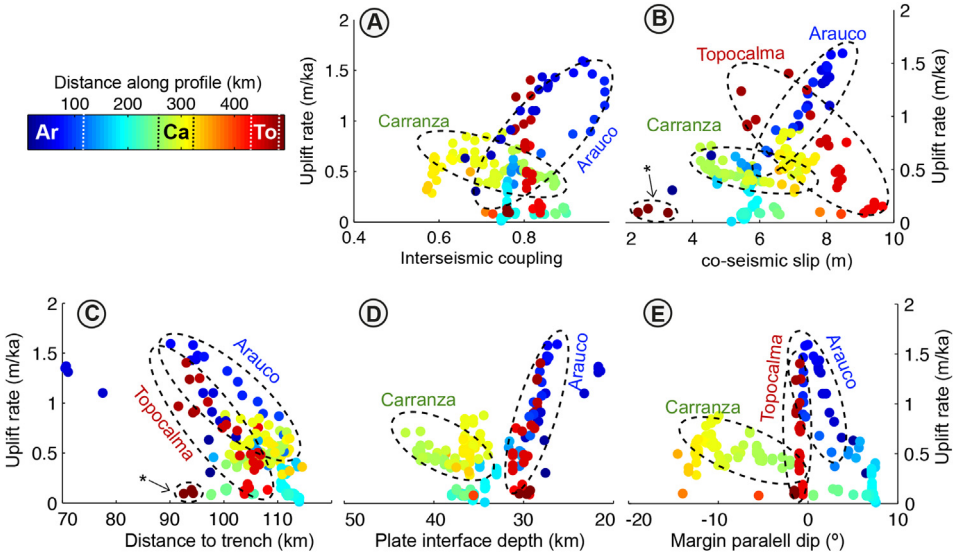

Fig. 13. Comparison between permanent uplift rates estimated from marine terraces, interseismic and co-seismic face and geometric features of the margin extracted at the position of terrace shorelines. Points are color-coded by distance along profile, from south to north. Position of Arauco, Carranza and Topocalma along profile indicated by letters Ar, Ca and To, respectively. See text for discussion. (A) Comparison between pre-2010 interseismic coupling and uplift rates. Coupling expressed as fraction of plate convergence. Note tentative inverse correlation at Carranza, positive correlation at Arauco, and no correlation at Topocalma. (B) Comparison between co-seismic slip and uplift rate. Note inverse correlations at Carranza and Topocalma and positive correlation at Arauco. (C) Comparison between distance to the trench and uplift rate. Note inverse correlation at Arauco and Topocalma. Outliers indicated by an asterisk are located at Navidad, beyond the northern boundary of the Maule rupture. High scatter at Carranza suggests no correlation. (D) Comparison between plate-interface depth and uplift rate. Note similarity at Topocalma and Arauco, and opposite trend at Carranza. (E) Comparison between margin-parallel dip angle of the Nazca Plate and uplift rate. Topocalma and Arauco are distributed in areas of flat to slightly positive dip associated with convex slab curvature. In turn, high uplift gradients at Carranza correlate with areas of concave slab curvature.

et al., 2005). However, to date no direct evidence of basal accretion has been documented by geophysical studies along the Chile margin. Alternatively, these long-wavelength structures may be related to oblique plate convergence and margin-parallel motion of forearc slivers in the upper plate as inferred at Arauco (Melnick et al., 2009) and also at the latitude of the Maipo orocline in the Main Cordillera (Lavenu and Cembrano, 1999).

Zones of rapid coastal uplift inferred from marine terraces have been commonly associated with subducted bathymetric features such as ridges, fracture zones and seamounts (e.g. Taylor et al., 1987; Macharé and Ortlieb, 1992). However, besides the subdued Mocha Fracture Zone no major oceanic features enter the subduction zone in the Maule segment (Fig. 1B). The Mocha Fracture is very narrow and has only ~200 m of associated relief, and it is thus considered unlikely to have an influence on the broad patterns of coastal uplift at Arauco (also see discussion in Melnick et al. (2009).

The epicenter of the Maule earthquake was located immediately south of Carranza (Fig. 1A), above a zone of high seismic velocity in the upper plate correlated with a positive gravity anomaly, interpreted to be associated with a subducted seamount with several kilometers of relief; this seamount is thought to have facilitated initiation of the rupture sequence (Hicks et al., 2012). However, we found low uplift rates (0.1–0.3 m/ka) along ~30 km of coast above the high-velocity region, suggesting that if a seamount had been subducted at this location, it must have detached from the lower plate more than ~125 ka ago.

5.2. Relationships between earthquake barriers and permanent deformation patterns

The three areas of rapid uplift along the Maule rupture approximately coincide with the boundaries of at least 8 historic earthquakes, despite uncertainties in their rupture zone terminations (Fig. 14A). For instance, Topocalma at the northern boundary of the 2010 Maule earthquake was also the limit of the 1751 (M~8.8), 1835 (M~8.5), 1906 (M8.6), 1985 (M8.0), and probably the 1928 (M~8) earthquakes. Similarly, Arauco is at the northern boundary of the giant 1960 (M9.5) and at the southern limit of the 1751, 1835 and 2010 events, although with substantial overlap. The area of Carranza was the boundary for the 1928 and giant 1730 (M~9) earthquakes. However, there are certainly differences in the along-strike distance over which slip during these earthquakes overlapped that may hint to variations in mechanical properties. The best-documented and largest zone of rupture overlap is at Arauco where slip during the 1960 and 2010 events occurred over a ~90-km-long zone. At Topocalma the overlap between historic earthquakes reached ~60 km (Fig. 14A). In turn, Carranza apparently has so far acted as a barrier only for ruptures that propagated from the north such as the 1730 event. Interestingly, the width of the zones of overlap is similar to the wavelength of the region of crustal upwarping and fast uplift rate, suggesting they are related to similar processes.

The nature of these earthquake boundaries is not yet understood. Melnick et al. (2009) proposed that a sharp gradient in petrophysical properties of the upper plate across the Lanalhue Fault, which juxtaposes different rock units, might be responsible for causing an inhomogenous earthquake barrier at Arauco. However, Haberland et al. (2009) found no major changes in seismic velocities and vp/vs ratios across this fault, suggesting that petrophysical conditions do not vary significantly. Thus, other crustal-scale processes probably associated with the rather broad patterns of crustal upwarping at Arauco and Topocalma should be responsible for arresting the propagation of megathrust ruptures across these regions. The changes in the curvature of the megathrust might act as geometric or inhomogeneous barriers that arrest propagation of megathrust ruptures. In addition, underplating of trench sediments at curved sectors of the plate interface could induce local changes in the frictional behavior of the megathrust accounting for the segmentation of earthquake ruptures.

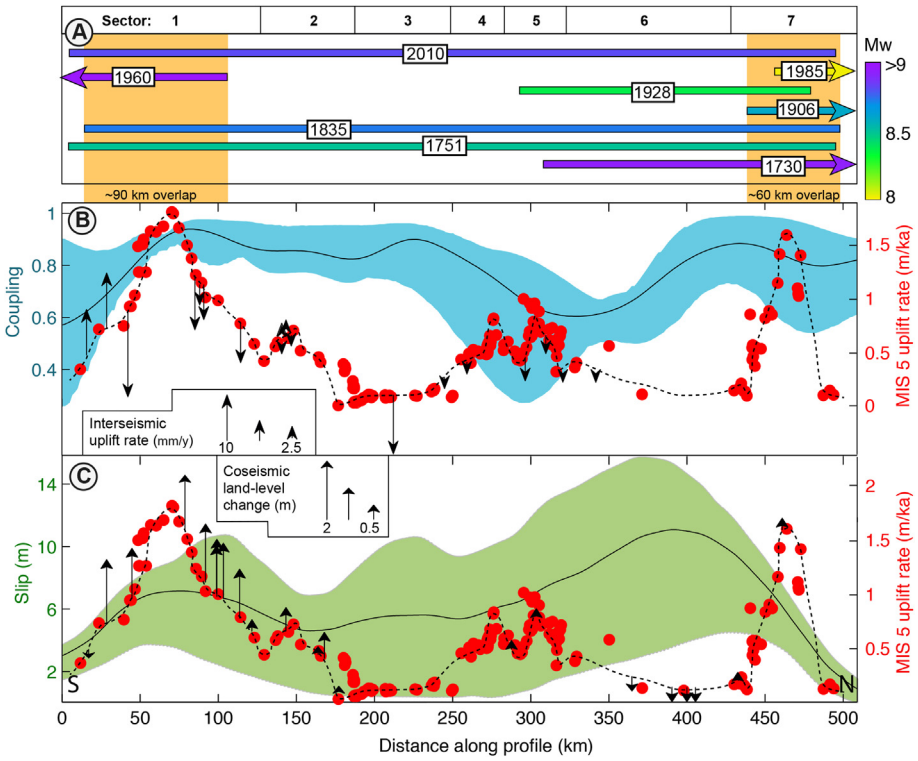

Fig. 14. Permanent and seismic-cycle deformation patterns along the Maule rupture. The area used for topography, coupling and slip swaths is indicated in Fig. 1A. (A) Rupture length of historical earthquakes color-coded by magnitude (from sources in the text), overlapping areas at Arauco and Topocalma discussed in the text highlighted by orange rectangles. (B) Swath profile of pre-2010 earthquake interseismic coupling (Moreno et al., 2010) and MIS-5 uplift rates. Arrows indicates the GPS velocity measured between 2004 and 2008 (Moreno et al., 2010; Metois et al., 2012). (C) Swath profile of Maule earthquake co-seismic slip (Moreno et al., 2012) with MIS-5 uplift rates, the arrows indicates co-seismic land-level changes (Farias et al., 2010; Melnick et al., 2012a). (For interpretation of the references to color in this figure legend, the reader is referred to the web version of this article.)

The longer wavelength of the bending zone affecting the megathrust and crust at Arauco with respect to Topocalma might explain the higher efficiency to restrain earthquake ruptures of the former, as suggested by historical records. Along these lines, only rupture propagation associated with two historical earthquakes terminated at Carranza (Fig. 14A), where the zone of high uplift is of even shorter wavelength and rather associated with discrete crustal faults. Areas of low or reduced coupling have been associated with intersegment regions that separate areas dominated by velocity-weakening frictional behavior at the interplate (Hetland and Simons, 2010). Carranza might be such a velocity-weakening dominated region whose capability of restraining rupture propagation will depend on the degree of interseismic coupling (Kaneko et al., 2010). Thus, lower interseismic coupling at Carranza with respect to the pre-2010 rate might have led to arrest rupture propagation of the 1730 event.

The existence of discrete seismotectonic blocks and barriers to rupture propagation along the south-central Chile margin is similar to observations from other subduction zones. Earthquake barriers have been commonly associated with lower or upper-plate anomalies. For example, Shennan et al. (2009), Audin et al. (2008), and Collot et al. (2004) related earthquake-rupture segmentation to upper-plate structures in Alaska, southern Peru, and Ecuador-Colombia, respectively. Along the same lines, Perfettini et al. (2010), Subarya et al. (2006) and Bilek et al. (2003) related bathymetric anomalies to sustained earthquake-rupture barriers in central Peru, Sumatra and Costa Rica, respectively. However, segmentation patterns in subduction zones do not seem to follow a unique pattern, because in some cases earthquakes are not constrained by structural features and rupture across segment boundaries. This has been observed in the Solomon islands (Taylor et al., 2008), Japan (Nanayama et al., 2003), and in Chile during the 1730 (M~9) earthquake (Udías et al., 2012). The latter ruptured across the area where the Juan Fernandez Ridge intersects the continental margin, illustrating the ambiguous role of inferred lower-plate earthquake barriers. Segmentation of historical ruptures along the Maule region coincides with patterns of permanent deformation and the overall geometric characteristics of the forearc, which are ultimately reflected in the upper plate.

Normal faults in forearc regions have been commonly related to megathrust ruptures (e.g. Loveless et al., 2010; Sherrod and Gomberg, 2014). Farías et al. (2011) and Ryder et al. (2012) proposed that faults between Pichilemu and Topocalma accommodate interseismic shortening by reverse motion and associated zones of wide folding. In their interpretation these structures are reactivated as normal faults by stress transferred from great earthquakes, as postulated for the region along the Pichilemu fault after the Maule earthquake. However, the 60-km width of the anticline at Topocalma is difficult to account for by reverse or normal faulting, and should rather result from deeper-seated processes such as margin-parallel shortening or underplating of subducted sediments. The Pelluhue and Carranza faults are also favorably oriented to slip as a result of stress transfer during slip in the northern patch of the Maule rupture. Thus, the arc-shaped pattern formed by the Pelluhue and Carranza faults in the south and the Pichilemu Fault in the north (Fig. 1B) could indicate that the high-slip northern patch of the Maule earthquake is a persistent feature characteristic of many earthquake cycles.

5.3. Comparison of seismic cycle and permanent deformation patterns

We tested whether deformation patterns at the time scale of the seismic cycle are correlated with the distribution of permanent deformation along the Maule rupture by directly comparing interseismic coupling measured in the decade before the earthquake with deformation during the earthquake and our estimates from MIS 5 marine terraces. Both co-seismic slip and interseismic coupling are distributed in two patches with different degrees of correlations with uplift rates deduced from marine terraces (Figs. 1A, 14B and C).

The comparison of co-seismic vertical displacements, based on intertidal fauna (Farias et al., 2010; Melnick et al., 2012a), with permanent uplift rates shows that these parameters are correlated mostly at Arauco and partly also at Topocalma (Fig. 14C). In the central part of the rupture, coastal subsidence occurred in an area of low uplift rates (Sector 6 and 7). Interseismic vertical velocities based on GPS measurements between 2004 and 2008 (Metois et al., 2012; Moreno et al., 2012) show subsidence at sites close to the trench along the Arauco Peninsula where the highest magnitudes of coseismic emergence were registered. However, the remaining sectors of the Maule coast appear to have been located near the interseismic hinge line.

A direct comparison of coseismic slip and interseismic coupling with permanent uplift rates at the location of the shoreline angles shows different relationships along the rupture zone (Fig. 13A and B). At Arauco slip and coupling exhibit a certain degree of correlation with uplift rate, suggesting permanent deformation may accumulate during great earthquakes. Arauco was uplifted during both the 1960 (M9.5) and 2010 Maule earthquakes (Plafker and Savage, 1970) (Melnick et al., 2012a), and thus the high permanent uplift rates might result from cumulative effect of ruptures from these two neighboring segments. Uplift rate and coupling are inversely correlated at Carranza but not correlated at Topocalma (Fig. 13A). Similarly, no clear correlation can be inferred between uplift rate and slip at these two sites (Fig. 13B). At Carranza an alternative source of permanent uplift might be deduced from the 2012 Constitución (M7.0) earthquake that caused slip along deeper portions of the plate boundary (39 km) resulting in ~15 cm of uplift (Ruiz et al., 2013) in an area that subsided ~5 cm during the Maule earthquake. This suggests that a portion of the permanent uplift might be accumulated by such deep events that occur during the post- and inter-seismic phases.

6. Conclusions

We deciphered and compared the pattern of permanent coastal deformation estimated from emerged marine terraces and seismic-cycle deformation along the 2010 Maule earthquake rupture zone of south-central Chile. We estimated uplift rates from 170 measurements of shoreline angles interpreted from high-resolution topographic data, tying the marine terrace chronology by means of 12 IRSL ages, stratigraphy and geomorphic mapping, and correlating them with different levels of the Marine Isotope Stages (MIS) 5e and 5c to obtain a long-term temporal and spatial signal of forearc deformation.

The mean terrace uplift rate along the entire Maule rupture of 0.50 m/ka is exceeded at Arauco (1.59 m/ka), Carranza (0.85 m/ka) and Topocalma (1.35 m/ka), located at the southern, central, and northern sectors of the 2010 rupture. These three rapidly uplifting sectors are characterized by different structural settings. The Arauco and Topocalma peninsulas are both located at the boundaries of the rupture and are characterized by broad antiformal structures with wavelengths of ~90 and ~60 km, respectively. Instead, Carranza is located at the center of the rupture zone and characterized by moderate uplift rates, sharp offsets across normal faults and short-wavelength flexures related to the elastic response of crustal faulting. These three areas coincide with the spatial limit of at least 8 historical megathrust ruptures (M8-9.5). We argue that these three areas can be understood as earthquake barriers, where overall deformation patterns, both at seismic-cycle and longer timescales, are controlled by the morphotectonic and geometric characteristics of the margin. These conclusions are based on the following arguments:

1. The boundaries of the Maule rupture spatially coincide with the symmetry axis of the Maipo and Arauco oroclines. These two features can be traced across the entire Andean margin, from fore-to back-arc, and have been active over the past few million years.
2. The long-wavelength zones of upwarping at Arauco and Topocalma are likely associated with deep-seated sources probably along the plate interface and/or the entire crust. We suggest that these zones might be associated with basal accretion of subducted trench sediments or with margin-parallel shortening resulting from oroclinal bending and motion of forearc slivers driven by oblique plate convergence.
3. The zones of rapid uplift and broad upwarping at Arauco and Topocalma coincide with the boundaries of historic earthquake ruptures. We infer that deformation of the upper plate might have played a role in the propagation of megathrust earthquakes in both regions. Instead, Carranza seems to arrest certain types of ruptures, possibly as a result of reduced interseismic coupling.
4. Fast coastal uplift at Topocalma and Arauco occurs in regions where the plate interface is shallower than elsewhere along the Maule rupture, and where coseismic slip is to a certain degree correlated with long-term uplift rates. This suggests that permanent deformation in these regions is accumulated during great earthquakes. In turn, in regions where the subducting slab is deeper, i.e. areas that are located farther inland from the trench, such as Carranza, show inverse relationships between long-term uplift rate and interseismic coupling, suggesting they might rise permanently during the interseismic period.

Acknowledgments

This study was developed within the framework of the project MARISCOS (MAule eaRthquake: Integration of Seismic Cycle Observations and Structural investigations) project financed by the German Science Foundation (DFG), grant STR 373/30-1. DM was supported by DFG grant ME 3157/2-2. We thank Kenneth Fisk, for his essential logistics and support during the two 45-days field campaigns developed between 2012 and 2013. Kevin Pedoja, Andrés Tassara, Rolando Armijo, and Patricio Zambrano are thanked for their insights into the relationships between marine terraces, tectonics and earthquakes. Two anonymous reviewers provided valuable comments. The LiDAR data was obtained from Markus Rombach and Digimapas Chile.

Appendix A. Supplementary data

Supplementary data related to this article can be found at http://dx.doi.org/10.1016/j.quascirev.2015.01.005.

References

Anderson, R., Densmore, A., Ellist, M., 1999. The generation and degradation of marine terraces. Basin Res. 11, 7–19.

Ando, M., 1975. Source mechanisms and tectonic significance of historical earthquakes along the Nankai Trough, Japan. Tectonophysics 27, 119–140.
Angermann, D., Klotz, J., Reigber, C., 1999. Space-geodetic estimation of the Nazca-South America euler vector. Earth Planet. Sci. Lett. 171, 329–334.
Araya-Vergara, J.F., 1976. Reconocimiento de tipos e individuos geomorfológicos regionales en la costa de Chile. Inf. Geogr. (Chile) 23, 9–30.
Aron, F., Allmendinger, R.W., Cembrano, J., González, G., Yañez, G., 2013. Permanent fore-arc extension and seismic segmentation: Insights from the 2010 Maule earthquake, Chile. J. Geophys. Res. Solid Earth 118, 724–739.
Ashby, J.R., Ku, T., Minch, J.A., 1987. Uranium series ages of corals from the upper Pleistocene Mulege terrace, Baja California Sur, Mexico. Geology 15, 139–141.
Audin, L., Lacan, P., Tavera, H., Bondoux, F., 2008. Upper plate deformation and seismic barrier in front of Nazca subduction zone: the Chololo Fault System and active tectonics along the Coastal Cordillera, southern Peru. Tectonophysics 459, 174–185.
Bangs, N.L., Cande, S.C., 1997. Episodic development of a convergent margin inferred from structures and processes along the southern Chile margin. Tectonics 16, 489–503.
Barrientos, S., 1987. Is the Pichilemu-Talcahuano (Chile) a seismic gap. Seismol. Res. Lett. 61, 43–48.
Barrientos, S.E., 1988. Slip distribution of the 1985 Central Chile earthquake. Tectonophysics 145, 225–241.
Beck, S., Barrientos, S., Kausel, E., Reyes, M., 1998. Source characteristics of historic earthquakes along the central Chile subduction Askew et Alzone. J. South Am. Earth Sci. 11, 115–129.
Bedford, J., Moreno, M., Baez, J.C., Lange, D., Tilmann, F., Rosenau, M., Heidbach, O., Oncken, O., Bartsch, M., Rietbrock, A., 2013. A high-resolution, time-variable afterslip model for the 2010 Maule Mw= 8.8, Chile megathrust earthquake. Earth Planet. Sci. Lett. 383, 26–36.
Berryman, K., Ota, Y., Hull, A., 1989. Holocene paleoseismicity in the fold and thrust belt of the Hikurangi subduction zone, eastern North Island, New Zealand. Tectonophysics 163, 185–195.
Bianca, M., Catalano, S., De Guidi, G., Gueli, A., Monaco, C., Ristuccia, G., Stella, G., Tortorici, G., Tortorici, L., Troja, S., 2011. Luminescence chronology of Pleistocene marine terraces of Capo Vaticano peninsula (Calabria, southern Italy). Quat. Int. 232, 114–121.
Bilek, S.L., Schwartz, S.Y., DeShon, H.R., 2003. Control of seafloor roughness on earthquake rupture behavior. Geology 31, 455–458.
Bohm, M., Lüth, S., Echtler, H., Asch, G., Bataille, K., Bruhn, C., Rietbrock, A., Wigger, P., 2002. The Southern Andes between 36° and 40°S latitude: seismicity and average seismic velocities. Tectonophysics 356, 275–289.
Bonnardot, M.-A., Hassani, R., Tric, E., Ruellan, E., Régnier, M., 2008. Effect of margin curvature on plate deformation in a 3-D numerical model of subduction zones. Geophys. J. Int. 173, 1084–1094.
Bookhagen, B., Echtler, H.P., Melnick, D., Strecker, M.R., Spencer, J.Q.G., 2006. Using uplifted Holocene beach berms for paleoseismic analysis on the Santa María Island, south-central Chile. Geophys. Res. Lett. 33, L15302.
Bowles, C.J., Cowgill, E., 2012. Discovering marine terraces using airborne LiDAR along the Mendocino-Sonoma coast, northern California. Geosphere 8, 386–402.
Bradley, W., Griggs, G., 1976. Form, genesis, and deformation of central California wave-cut platforms. Geol. Soc. Am. Bull. 87, 433–449.
Bradley, W.C., 1957. Origin of marine-terrace deposits in the Santa Cruz area, California. Geol. Soc. Am. Bull. 68, 421–444.
Brooks, B.A., Bevis, M., Smalley, R., Kendrick, E., Manceda, R., Lauria, E., Maturana, R., Araujo, M., 2003. Crustal motion in the Southern Andes (26-36 S): do the Andes behave like a microplate? Geochem. Geophys. Geosyst. 4.
Campos, J., Hatzfeld, D., Madariaga, R., Lopez, G., Kausel, E., Zollo, A., Iannacone, G., Fromm, R., Barrientos, S., Lyon-Caen, H., 2002. A seismological study of the 1835 seismic gap in south-central Chile. Phys. Earth Planet. Inter. 132, 177–195.
Cecioni, G., 1983. Chanco Formation, a potential Cretaceous reservoir, central Chile. J. Pet. Geol. 6, 89–93.
Chen, M.-C., Frohlich, C., Taylor, F.W., Burr, G., Van Ufford, A.Q., 2011. Arc segmentation and seismicity in the Solomon Islands arc, SW Pacific. Tectonophysics 507, 47–69.
Chlieh, M., Avouac, J.-P., Hjorleifsdottir, V., Song, T.-R.A., Ji, C., Sieh, K., Sladen, A., Hebert, H., Prawirodirdjo, L., Bock, Y., 2007. Coseismic slip and afterslip of the great Mw 9.15 Sumatra-Andaman earthquake of 2004. Bull. Seismol. Soc. Am. 97, S152–S173.
Cifuentes, I.L., 1989. The 1960 Chilean earthquakes. J. Geophys. Res. Solid Earth 94, 665–680.
Cisternas, M., Ely, L., Wesson, R., Pilarckzic, J., Gorigoitia, N., Dura, T., Melnick, D., Carvajal, M., 2014. The 1730 and 1751 Chilean earthquakes: two major contributors to the seismically prolific 18th century along the Pacific Coast of the Americas. In: SSA Annual Meeting, Anchorage, Alaska.
Collot, J.-Y., Marcaillou, B., Sage, F., Michaud, F., Agudelo, W., Charvis, P., Graindorge, D., Gutscher, M.-A., Spence, G., 2004. Are rupture zone limits of great subduction earthquakes controlled by upper plate structures? Evidence from multichannel seismic reflection data acquired across the northern Ecuador-southwest Colombia margin. J. Geophys. Res. Solid Earth (1978-2012) 109.
Darwin, C., 1851. Geological Observations of South America. Smith, Elder, London.
Delouis, B., Nocquet, J.-M., Vallée, M., 2010. Slip distribution of the February 27, 2010 Mw = 8.8 Maule Earthquake, central Chile, from static and high-rate GPS, InSAR, and broadband teleseismic data. Geophys. Res. Lett. 37, L17305.
Dumas, B., Hoang, C.T., Raffy, J., 2006. Record of MIS 5 sea-level highstands based on U/Th dated coral terraces of Haiti. Quat. Int. 145, 106–118.
Dupré, W.R., 1984. Reconstruction of paleo-wave conditions during the late Pleistocene from marine terrace deposits, Monterey Bay, California. Mar. Geol. 60, 435–454.
Encinas, A., Herve, F., Villa-Martinez, R., Nielsen, S.N., Finger, K.L., Peterson, D.E., 2006a. Finding of a Holocene marine layer in Algarrobo (33° 22 ' S), central Chile. Implications for coastal uplift. Rev. Geol. De Chile 33, 339–345.
Encinas, A., Le Roux, J.P., Buatois, L.A., Nielsen, S.N., Finger, K.L., Fourtanier, E., Lavenu, A., 2006b. Nuevo esquema estratigrafico para los depositos marinos mio-pliocenos del area de Navidad (33 -34 30'S), Chile central. Rev. Geol. Chile 33, 221–246.
Farías, M., Charrier, R., Carretier, S., Martinod, J., Fock, A., Campbell, D., Cáceres, J., Comte, D., 2008. Late Miocene high and rapid surface uplift and its erosional response in the Andes of central Chile (33-35 S). Tectonics 27.
Farías, M., Comte, D., Roecker, S., Carrizo, D., Pardo, M., 2011. Crustal extensional faulting triggered by the 2010 Chilean earthquake: the Pichilemu Seismic Sequence. Tectonics 30, TC6010.
Farias, M., Vargas, G., Tassara, A., Carretier, S., Baize, S., Melnick, D., Bataille, K., 2010. Land-level changes produced by the Mw 8.8 2010 Chilean earthquake. Science 329, 916–916.
Galbraith, R.F., Roberts, R.G., Laslett, G., Yoshida, H., Olley, J.M., 1999. Optical dating of single and multiple grains of quartz from jinmium rock shelter, northern australia: part i, experimental design and statistical models*. Archaeometry 41, 339–364.
Gallen, S., Wegmann, K., Bohnenstiehl, D., Pazzaglia, F., Brandon, M., Fassoulas, C., 2014. Active simultaneous uplift and margin-normal extension in a forearc high, Crete, Greece. Earth Planet. Sci. Lett. 398, 11–24.
Geersen, J., Behrmann, J.H., Völker, D., Krastel, S., Ranero, C.R., Diaz-Naveas, J., Weinrebe, W., 2011. Active tectonics of the South Chilean marine fore arc (35°S–40°S). Tectonics 30, TC3006.
Gilbert, G.K., 1890. Lake Bonneville. In: United States Geological Survey.
Glodny, J., Echtler, H., Collao, S., Ardiles, M., Burón, P., Figueroa, O., 2008. Differential Late Paleozoic active margin evolution in South-Central Chile (37°S-40°S) -The Lanalhue Fault Zone. J. South Am. Earth Sci. 26, 397–411.
Glodny, J., Lohrmann, J., Echtler, H., Gräfe, K., Seifert, W., Collao, S., Figueroa, O., 2005. Internal dynamics of a paleoaccretionary wedge: insights from combined isotope tectonochronology and sandbox modelling of the South-Central Chilean forearc. Earth Planet. Sci. Lett. 231, 23–39.
Gonzalez, E., 1990. Hydrocarbon Resources in the Coastal Zone of Chile.
Gurrola, L.D., Keller, E.A., Chen, J.H., Owen, L.A., Spencer, J.Q., 2014. Tectonic geomorphology of marine terraces: Santa Barbara fold belt, California. Geol. Soc. Am. Bull. 126, 219–233.
Haberland, C., Rietbrock, A., Lange, D., Bataille, K., Dahm, T., 2009. Structure of the seismogenic zone of the southcentral Chilean margin revealed by local earthquake traveltime tomography. J. Geophys. Res. Solid Earth (1978-2012) 114.
Hanks, T.C., Bucknam, R.C., Lajoie, K.R., Wallace, R.E., 1984. Modification of wave-cut and faulting-controlled landforms. J. Geophys. Res. Solid Earth (1978-2012) 89, 5771–5790.
Hearty, P.J., Hollin, J.T., Neumann, A.C., O'Leary, M.J., McCulloch, M., 2007. Global sea-level fluctuations during the Last Interglaciation (MIS 5e). Quat. Sci. Rev. 26, 2090–2112.
Hetland, E., Simons, M., 2010. Post-seismic and interseismic fault creep II: transient creep and interseismic stress shadows on megathrusts. Geophys. J. Int. 181, 99–112.
Hicks, S.P., Rietbrock, A., Haberland, C.A., Ryder, I.M.A., Simons, M., Tassara, A., 2012. The 2010 Mw 8.8 Maule, Chile earthquake: nucleation and rupture propagation controlled by a subducted topographic high. Geophys. Res. Lett. 39, L19308.
Huntley, D., Baril, M., 1997. The K content of the K-feldspars being measured in optical dating or in thermoluminescence dating. Anc. TL 15, 11–13.
Jackson, J.A., Mehl, J.P., Neuendorf, K.K., 2005. Glossary of Geology. Springer.
Jaramillo, E., Dugan, J.E., Hubbard, D.M., Melnick, D., Manzano, M., Duarte, C., Campos, C., Sanchez, R., 2012. Ecological implications of extreme events: footprints of the 2010 earthquake along the Chilean coast. PloS one 7, e35348.
Jara-Muñoz, J., Melnick, D., 2015. Unraveling sea-level variations and tectonic uplift in wave-built marine terraces, Santa María Island. Chile. Quat. Res. 83, 216–228.
Kaizuka, S., Matsuda, T., Nogami, M., Yonekura, N., 1973. Quaternary Tectonic and Recent Seismic Crustal Movements in the Arauco Peninsula and its Environs, Central Chile. Geographical reports of Tokyo Metropolitan University 8, pp. 1–49.
Kaneko, Y., Avouac, J.-P., Lapusta, N., 2010. Towards inferring earthquake patterns from geodetic observations of interseismic coupling. Nat. Geosci. 3, 363–369.
Kato, T.T., 1985. Pre-Andean orogenesis in the Coast Ranges of central Chile. Geol. Soc. Am. Bull. 96, 918–924.
Khazaradze, G., Klotz, J., 2003. Short-and long-term effects of GPS measured crustal deformation rates along the south central Andes. J. Geophys. Res. Solid Earth (1978-2012) 108.
Kiser, E., Ishii, M., 2011. The 2010 Mw 8.8 Chile earthquake: triggering on multiple segments and frequency-dependent rupture behavior. Geophys. Res. Lett. 38, L07301.
Klotz, J., Khazaradze, G., Angermann, D., Reigber, C., Perdomo, R., Cifuentes, O., 2001. Earthquake cycle dominates contemporary crustal deformation in Central and Southern Andes. Earth Planet. Sci. Lett. 193, 437–446.
Kölbl-Ebert, M., 1999. Observing orogeny e Maria Graham's account of the earthquake in Chile in 1822. Geologische Staatssammlung München, München, Germany.
Kukla, G.J., Bender, M.L., de Beaulieu, J.-L., Bond, G., Broecker, W.S., Cleveringa, P., Gavin, J.E., Herbert, T.D., Imbrie, J., Jouzel, J., 2002. Last interglacial climates. Quat. Res. 58, 2–13.

Lajoie, K.R., 1986. Coastal tectonics. Act. Tect. 95–124.
Lange, D., Tilmann, F., Barrientos, S.E., Contreras-Reyes, E., Methe, P., Moreno, M., Heit, B., Agurto, H., Bernard, P., Vilotte, J.-P., Beck, S., 2012. Aftershock seismicity of the 27 February 2010 Mw 8.8 Maule earthquake rupture zone. Earth Planet. Sci. Lett. 317–318, 413–425.
Lavenu, A., Cembrano, J., 1999. Compressional-and transpressional-stress pattern for Pliocene and Quaternary brittle deformation in fore arc and intra-arc zones (Andes of Central and Southern Chile). J. Struct. Geol. 21, 1669–1691.
Limber, P.W., Murray, A.B., 2011. Beach and sea-cliff dynamics as a driver of long-term rocky coastline evolution and stability. Geology 39, 1147–1150.
Lin, Y.-n.N., Sladen, A., Ortega-Culaciati, F., Simons, M., Avouac, J.-P., Fielding, E.J., Brooks, B.A., Bevis, M., Genrich, J., Rietbrock, A., Vigny, C., Smalley, R., Socquet, A., 2013. Coseismic and postseismic slip associated with the 2010 Maule Earthquake, Chile: characterizing the Arauco Peninsula Barrier Effect. J. Geophys. Res. Solid Earth 118, 3142–3159.
Lomnitz, C., 2004. Major earthquakes of Chile: a historical survey, 1535-1960. Seismol. Res. Lett. 75, 368–378.
Lorito, S., Romano, F., Atzori, S., Tong, X., Avallone, A., McCloskey, J., Cocco, M., Boschi, E., Piatanesi, A., 2011. Limited overlap between the seismic gap and coseismic slip of the great 2010 Chile earthquake. Nat. Geosci. 4, 173–177.
Loveless, J.P., Allmendinger, R.W., Pritchard, M.E., González, G., 2010. Normal and reverse faulting driven by the subduction zone earthquake cycle in the northern Chilean fore arc. Tectonics 29.
Loveless, J.P., Meade, B.J., 2011. Spatial correlation of interseismic coupling and coseismic rupture extent of the 2011 MW= 9.0 Tohoku-oki earthquake. Geophys. Res. Lett. 38.
Macharé, J., Ortlieb, L., 1992. Plio-Quaternary vertical motions and the subduction of the Nazca Ridge, central coast of Peru. Tectonophysics 205, 97–108.
Mardones, M., Jaque, E., 1991. Geomorfología del Valle del Río Laja, Extensos de Ponencias y Seminarios. Servicio Geografico Militar, Santiago, Chile, p. 6.
Marquardt, C., Lavenu, A., Ortlieb, L., Godoy, E., Comte, D., 2004. Coastal neotectonics in Southern Central Andes: uplift and deformation of marine terraces in Northern Chile (27 S). Tectonophysics 394, 193–219.
Mauz, B., 1999. Late Pleistocene records of littoral processes at the Tyrrhenian Coast (Central Italy): depositional environments and luminescence chronology. Quat. Sci. Rev. 18, 1173–1184.
Melnick, D., Bookhagen, B., Echtler, H., Strecker, M., 2006. Coastal deformation and great subduction earthquakes, Isla Santa María, Chile (37°S). Geol. Soc. Am. Bull. 118, 1463–1480.
Melnick, D., Bookhagen, B., Strecker, M.R., Echtler, H.P., 2009. Segmentation of megathrust rupture zones from fore-arc deformation patterns over hundreds to millions of years, Arauco peninsula, Chile. J. Geophys. Res. Solid Earth 114, B01407.
Melnick, D., Cisternas, M., Moreno, M., Norambuena, R., 2012a. Estimating coseismic coastal uplift with an intertidal mussel: calibration for the 2010 Maule Chile earthquake (Mw 8.8). Quat. Sci. Rev. 42, 29–42.
Melnick, D., Echtler, H.P., 2006. Inversion of forearc basins in south-central Chile caused by rapid glacial age trench fill. Geology 34, 709–712.
Melnick, D., Moreno, M., Motagh, M., Cisternas, M., Wesson, R.L., 2012b. Splay fault slip during the Mw 8.8 2010 Maule Chile earthquake. Geology 40, 251–254.
Melosh, H., Raefsky, A., 1980. The dynamical origin of subduction zone topography. Geophys. J. R. Astron. Soc. 60, 333–354.
Merritts, D., Chadwick, O., Hendricks, D., 1991. Rates and processes of soil evolution on uplifted marine terraces, northern California. Geoderma 51, 241–275.
Metois, M., Socquet, A., Vigny, C., 2012. Interseismic coupling, segmentation and mechanical behavior of the central Chile subduction zone. J. Geophys. Res. Solid Earth (1978-2012) 117.
Mordojovich, C., 1981. Sedimentary basins of Chilean Pacific Offshore. In: Halbouty, M.T. (Ed.), Energy Resources of the Pacific Region, AAPG Studies in Geology, pp. 63–82.
Moreno, M., Melnick, D., Rosenau, M., Baez, J., Klotz, J., Oncken, O., Tassara, A., Chen, J., Bataille, K., Bevis, M., Socquet, A., Bolte, J., Vigny, C., Brooks, B., Ryder, I., Grund, V., Smalley, B., Carrizo, D., Bartsch, M., Hase, H., 2012. Toward understanding tectonic control on the Mw 8.8 2010 Maule Chile earthquake. Earth Planet. Sci. Lett. 321–322, 152–165.
Moreno, M., Rosenau, M., Oncken, O., 2010. 2010 Maule earthquake slip correlates with pre-seismic locking of Andean subduction zone. Nature 467, 198–202.
Moreno, M.S., Bolte, J., Klotz, J., Melnick, D., 2009. Impact of megathrust geometry on inversion of coseismic slip from geodetic data: application to the 1960 Chile earthquake. Geophys. Res. Lett. 36.
Moreno, M.S., Klotz, J., Melnick, D., Echtler, H., Bataille, K., 2008. Active faulting and heterogeneous deformation across a megathrust segment boundary from GPS data, south central Chile (36–39°S). Geochem. Geophys. Geosyst. 9, Q12024.
Muhs, D.R., 2002. Evidence for the timing and duration of the last interglacial period from high-precision uranium-series ages of corals on tectonically stable coastlines. Quat. Res. 58, 36–40.
Muhs, D.R., Kelsey, H.M., Miller, G.H., Kennedy, G.L., Whelan, J.F., McInelly, G.W., 1990. Age estimates and uplift rates for Late Pleistocene marine terraces: southern Oregon portion of the Cascadia Forearc. J. Geophys. Res. 95, 6685–6698.
Nanayama, F., Satake, K., Furukawa, R., Shimokawa, K., Atwater, B.F., Shigeno, K., Yamaki, S., 2003. Unusually large earthquakes inferred from tsunami deposits along the Kuril trench. Nature 424, 660–663.
Nelson, A.R., Manley, W.F., 1992. Holocene coseismic and aseismic uplift of Isla Mocha, south-central Chile. Quat. Int. 15, 61–76.
Okal, E.A., 2005. A re-evaluation of the great Aleutian and Chilean earthquakes of 1906 August 17. Geophys. J. Int. 161, 268–282.
Ozawa, S., Nishimura, T., Suito, H., Kobayashi, T., Tobita, M., Imakiire, T., 2011. Coseismic and postseismic slip of the 2011 magnitude-9 Tohoku-Oki earthquake. Nature 475, 373–376.
Pedoja, K., Husson, L., Johnson, M.E., Melnick, D., Witt, C., Pochat, S.P., Nexer, M.L., Delcaillau, B., Pinegina, T., Poprawski, Y., Authemayou, C., Elliot, M., Regard, V., Garestier, F., 2014. Coastal staircase sequences reflecting sea-level oscillations and tectonic uplift during the Quaternary and Neogene. Earth-Sci. Rev. 132, 13–38.
Pedoja, K., Husson, L., Regard, V., Cobbold, P.R., Ostanciaux, E., Johnson, M.E., Kershaw, S., Saillard, M., Martinod, J., Furgerot, L., 2011. Relative sea-level fall since the last interglacial stage: are coasts uplifting worldwide? Earth-Sci. Rev. 108, 1–15.
Perfettini, H., Avouac, J.-P., Tavera, H., Kositsky, A., Nocquet, J.-M., Bondoux, F., Chlieh, M., Sladen, A., Audin, L., Farber, D.L., 2010. Seismic and aseismic slip on the central Peru megathrust. Nature 465, 78–81.
Plafker, G., Savage, J., 1970. Mechanism of the Chilean earthquakes of May 21 and 22, 1960. Geol. Soc. Am. Bull. 81, 1001–1030.
Pollitz, F.F., Brooks, B., Tong, X., Bevis, M.G., Foster, J.H., Bürgmann, R., Smalley, R., Vigny, C., Socquet, A., Ruegg, J.-C., 2011. Coseismic slip distribution of the February 27, 2010 Mw 8.8 Maule, Chile earthquake. Geophys. Res. Lett. 38.
Potter, E.-K., Esat, T.M., Schellmann, G., Radtke, U., Lambeck, K., McCulloch, M.T., 2004. Suborbital-period sea-level oscillations during marine isotope substages 5a and 5c. Earth Planet. Sci. Lett. 225, 191–204.
Prescott, J., Hutton, J.T., 1994. Cosmic ray contributions to dose rates for luminescence and ESR dating: large depths and long-term time variations. Radiat. Meas. 23, 497–500.
Pulido, N., Yagi, Y., Kumagai, H., Nishimura, N., 2011. Rupture process and coseismic deformations of the 27 February 2010 Maule earthquake. Chile. Earth Planets Space 63, 955–959.
Rehak, K., Strecker, M.R., Echtler, H.P., 2008. Morphotectonic segmentation of an active forearc, 37-41° S, Chile. Geomorphology 94, 98–116.
Rohling, E., Grant, K., Bolshaw, M., Roberts, A., Siddall, M., Hemleben, C., Kucera, M., 2009. Antarctic temperature and global sea level closely coupled over the past five glacial cycles. Nat. Geosci. 2, 500–504.
Rosenbloom, N.A., Anderson, R.S., 1994. Hillslope and channel evolution in a marine terraced landscape, Santa Cruz, California. J. Geophys. Res. Solid Earth (1978-2012) 99, 14013–14029.
Ruegg, J.C., Rudloff, A., Vigny, C., Madariaga, R., de Chabalier, J.B., Campos, J., Kausel, E., Barrientos, S., Dimitrov, D., 2009. Interseismic strain accumulation measured by GPS in the seismic gap between Constitución and Concepción in Chile. Phys. Earth Planet. Inter. 175, 78–85.
Ruiz, S., Grandin, R., Dionicio, V., Satriano, C., Fuenzalida, A., Vigny, C., Kiraly, E., Meyer, C., Baez, J.C., Riquelme, S., 2013. The Constitucion earthquake of 25 March 2012: a large aftershock of the Maule earthquake near the bottom of the seismogenic zone. Earth Planet. Sci. Lett. 377, 347–357.
Ryder, I., Rietbrock, A., Kelson, K., Bürgmann, R., Floyd, M., Socquet, A., Vigny, C., Carrizo, D., 2012. Large extensional aftershocks in the continental forearc triggered by the 2010 Maule earthquake, Chile. Geophys. J. Int. 188, 879–890.
Saillard, M., Hall, S.R., Audin, L., Farber, D.L., Hérail, G., Martinod, J., Regard, V., Finkel, R.C., Bondoux, F., 2009. Non-steady long-term uplift rates and Pleistocene marine terrace development along the Andean margin of Chile (31°S) inferred from 10Be dating. Earth Planet. Sci. Lett. 277, 50–63.
Scott, A.T., Pinter, N., 2003. Extraction of coastal terraces and shoreline-angle elevations from digital terrain models, Santa Cruz and Anacapa Islands, California. Phys. Geogr. 24, 271–294.
Shackleton, N.J., Sanchez-Goni, M.F., Pailler, D., Lancelot, Y., 2003. Marine isotope substage 5e and the Eemian interglacial. Glob. Planet. Change 36, 151–155.
Shao, G., Li, X., Liu, Q., Zhao, X., Yano, T., Li, C., 2010. A Slip model of the Feb 27, 2010 Mw 8.9 Maule, Chile Earthquake. In: EGU General Assembly Conference Abstracts, p. 15704.
Shennan, I., Bruhn, R., Plafker, G., 2009. Multi-segment earthquakes and tsunami potential of the Aleutian megathrust. Quat. Sci. Rev. 28, 7–13.
Sherrod, B., Gomberg, J., 2014. Crustal earthquake triggering by prehistoric great earthquakes on subduction zone thrusts. J. Geophys. Res. Solid Earth 119, 1273–1294.
Stefer, S., Moernaut, J., Melnick, D., Echtler, H.P., Arz, H.W., Lamy, F., De Batist, M., Oncken, O., Haug, G.H., 2010. Forearc uplift rates deduced from sediment cores of two coastal lakes in south-central Chile. Tectonophysics 495, 129–143.
Steffen, D., Preusser, F., Schlunegger, F., 2009. OSL quartz age underestimation due to unstable signal components. Quat. Geochronol. 4, 353–362.
Subarya, C., Chlieh, M., Prawirodirdjo, L., Avouac, J.-P., Bock, Y., Sieh, K., Meltzner, A.J., Natawidjaja, D.H., McCaffrey, R., 2006. Plate-boundary deformation associated with the great Sumatra-Andaman earthquake. Nature 440, 46–51.
Suito, H., Freymueller, J.T., 2009. A viscoelastic and afterslip postseismic deformation model for the 1964 Alaska earthquake. J. Geophys. Res. Solid Earth (1978-2012) 114.
Tassara, A., Götze, H.J., Schmidt, S., Hackney, R., 2006. Three-dimensional density model of the Nazca plate and the Andean continental margin. J. Geophys. Res. Solid Earth (1978-2012) 111.
Taylor, F.W., Briggs, R.W., Frohlich, C., Brown, A., Hornbach, M., Papabatu, A.K., Meltzner, A.J., Billy, D., 2008. Rupture across arc segment and plate boundaries in the 1 April 2007 Solomons earthquake. Nat. Geosci. 1, 253–257.
Taylor, F.W., Frohlich, C., Lecolle, J., Strecker, M., 1987. Analysis of partially emerged corals and reef terraces in the central Vanuatu arc: comparison of

contemporary coseismic and nonseismic with Quaternary vertical movements. J. Geophys. Res. Solid Earth (1978-2012) 92, 4905–4933.
Tebbens, S.F., Cande, S.C., 1997. Southeast Pacific tectonic evolution from Early Oligocene to present. J. Geophys. Res. Solid Earth 102, 12061–12084.
Tong, X., Sandwell, D., Luttrell, K., Brooks, B., Bevis, M., Shimada, M., Foster, J., Smalley, R., Parra, H., Báez Soto, J.C., Blanco, M., Kendrick, E., Genrich, J., Caccamise, D.J., 2010. The 2010 Maule, Chile earthquake: downdip rupture limit revealed by space geodesy. Geophys. Res. Lett. 37, L24311.
Trenhaile, A., Pepper, D., Trenhaile, R., Dalimonte, M., 1998. Stacks and notches at Hopewell Rocks, New Brunswick, Canada. Earth Surf. Process. Landf. 23, 975–988.
Trenhaile, A.S., 2002. Modeling the development of marine terraces on tectonically mobile rock coasts. Mar. Geol. 341–361.
Udías, A., Madariaga, R., Buforn, E., Muñoz, D., Ros, M., 2012. The large Chilean historical earthquakes of 1647, 1657, 1730, and 1751 from contemporary documents. Bull. Seismol. Soc. Am. 102, 1639–1653.
Vargas, G., Farias, M., Carretier, S., Tassara, A., Baize, S., Melnick, D., 2011. Coastal uplift and tsunami effects associated to the 2010 M(w)8.8 Maule earthquake in Central Chile. Andean Geol. 38, 219–238.
Victor, P., Sobiesiak, M., Glodny, J., Nielsen, S., Oncken, O., 2011. Long-term persistence of subduction earthquake segment boundaries: evidence from Mejillones Peninsula, northern Chile. J. Geophys. Res. Solid Earth (1978-2012) 116.
Vigny, C., Rudloff, A., Ruegg, J.-C., Madariaga, R., Campos, J., Alvarez, M., 2009. Upper plate deformation measured by GPS in the Coquimbo Gap, Chile. Phys. Earth Planet. Inter. 175, 86–95.
Vigny, C., Socquet, A., Peyrat, S., Ruegg, J.-C., Métois, M., Madariaga, R., Morvan, S., Lancieri, M., Lacassin, R., Campos, J., Carrizo, D., Bejar-Pizarro, M., Barrientos, S., Armijo, R., Aranda, C., Valderas-Bermejo, M.-C., Ortega, I., Bondoux, F., Baize, S., Lyon-Caen, H., Pavez, A., Vilotte, J.P., Bevis, M., Brooks, B., Smalley, R., Parra, H., Baez, J.-C., Blanco, M., Cimbaro, S., Kendrick, E., 2011. The 2010 Mw 8.8 Maule megathrust earthquake of Central Chile, monitored by GPS. Science 332, 1417–1421.
Wang, K., 2007. Elastic and viscoelastic models of crustal deformation in subduction earthquake cycles. Seismogenic Zone Subduction Thrust Faults 540–575.
Watts, A., Daly, S., 1981. Long wavelength gravity and topography anomalies. Annu. Rev. Earth Planet. Sci. 9, 415–448.
Weber, G.E., 1990. Late Pleistocene Slip Rates on the San Gregorio Fault Zone at Point Ano Nuevo, San Mateo County, California. AAPG Pacific Section, pp. 193–203.
Yildirim, C., Melnick, D., Ballato, P., Schildgen, T.F., Echtler, H., Erginal, A.E., Kiyak, N.N.G., Strecker, M.R., 2013. Differential uplift along the northern margin of the Central Anatolian Plateau: inferences from marine terraces. Quat. Sci. Rev. 81, 12–28.
Yue, H., Lay, T., Rivera, L., An, C., Vigny, C., Tong, X., Báez Soto, J.C., 2014. Localized fault slip to the trench in the 2010 Maule, Chile Mw= 8.8 earthquake from joint inversion of high-rate GPS, teleseismic body waves, InSAR, campaign GPS, and tsunami observations. J. Geophys. Res. Solid Earth 119, 7786–7804.
Zazo, C., Goy, J.L., Dabrio, C.J., Bardají, T., Hillaire-Marcel, C., Ghaleb, B., González-Delgado, J.-Á., Soler, V., 2003. Pleistocene raised marine terraces of the Spanish Mediterranean and Atlantic coasts: records of coastal uplift, sea-level high-stands and climate changes. Mar. Geol. 194, 103–133.
Zecchin, M., Civile, D., Caffau, M., Roda, C., 2009. Facies and cycle architecture of a Pleistocene marine terrace (Crotone, southern Italy): a sedimentary response to late Quaternary, high-frequency glacio-eustatic changes. Sediment. Geol. 216, 138–157.